Experimental Study of Main Gas Ingestion and Purge Gas Egress Flow in Model Gas Turbine Stages

by

Jagdish Harihara Balasubramanian

A Thesis Presented in Partial Fulfillment
of the Requirements for the Degree
Master of Science

Approved November 2010 by the
Graduate Supervisory Committee:

Ramendra P Roy, Chair
Taewoo Lee
Patrick Phelan

ARIZONA STATE UNIVERSITY

December 2010

ABSTRACT

Efficient performance of gas turbines depends, among several parameters, on the mainstream gas entry temperature. At the same time, transport of this high temperature gas into the rotor-stator cavities of turbine stages affects the durability of rotor disks. This transport is usually countered by installing seals on the rotor and stator disk rims and by pressurizing the cavities by injecting air (purge gas) bled from the compressor discharge. The configuration of the rim seals influences the magnitude of main gas ingestion as well as the interaction of the purge gas with the main gas. The latter has aerodynamic and hub endwall heat transfer implications in the main gas path.

In the present work, experiments were performed on model single-stage and 1.5-stage axial-flow turbines. The turbines featured vanes, blades, and rim seals on both the rotor and stator disks. Three different rim seal geometries, viz., axially overlapping radial clearance rim seals for the single-stage turbine cavity and the 1.5-stage turbine aft cavity, and a rim seal with angular clearance for the single-stage turbine cavity were studied. In the single-stage turbine, an inner seal radially inboard in the cavity was also provided; this effectively divided the disk cavity into a rim cavity and an inner cavity. For the aft rotor-stator cavity of the 1.5-stage turbine, a labyrinth seal was provided radially inboard, again creating a rim cavity and an inner cavity. Measurement results of time-average main gas ingestion into the cavities using tracer gas (CO_2), and ensemble-averaged trajectories of the purge gas flowing out through the rim seal gap into the main gas path using particle image velocimetry are presented.

For both turbines, significant ingestion occurred only in the rim cavity. The inner cavity was almost completely sealed by the inner seal, at all purge gas flow rates for the single-stage turbine and at the higher purge gas flow rates for 1.5-stage turbine. Purge gas egress trajectory was found to depend on main gas and purge gas flow rates, the rim seal configuration, and the azimuthal location of the trajectory mapping plane with respect to the vanes.

DEDICATION

To Appa, Amma, Madhu, Sriram and Saket

ACKNOWLEDGMENTS

I take this opportunity to thank many people with whose help, this thesis work was realized. I sincerely thank Professor Ramendra P.Roy for accepting me into his research lab and guiding me throughout the course of this work. I thank Professor Taewoo Lee and Professor Patrick Phelan for having agreed to be on my committee.

Thanks to Dr Ding Wei-Zhou, Post-doctoral Research Associate at the Department of Mechanical and Aerospace Engineering for his guidance in the initial phase of this work. I would also like to thank my colleague Nihal U Junnarkar for his contribution to this work through his selfless involvement.

Many thanks to Leonard Montenegro, Senior Research Professional at the Department of Mechanical Engineering for his helpful and valuable suggestions during the course of this work. Thanks to Dr Michael J Murphy, (LEFT, ASU) for his helpful suggestions.

Special thanks to the personnel of the Engineering Technical Services, Dennis Golabiewski, Fred Sierra, Ben Schwatken and Martin Johnson for their help in putting together various assemblies and design insights.

Thanks are due to my friends Madusudanan, Rajesh, Siva, Jaiganesh, Sajesh and Chinmoy for their support and help.

TABLE OF CONTENTS

Page

LIST OF TABLES vii

LIST OF FIGURES viii

NOMENCLATURE xiii

CHAPTER

1 INTRODUCTION 1

1.1 Background 1

1.2 Literature Survey 2

1.3 Overview of the Present Work 6

2 TEST FACILITY AND EXPERIMENTS 7

2.1 Experimental Facility 7

2.1.1 Turbine Stages 10

2.2 Time-Average Static Gage Pressure Measurement 17

2.2.1 System Components 17

2.2.2 Experimental Procedure 20

2.3 Mainstream Gas Ingestion Measurement 21

2.3.1 System Components 21

2.3.2 Experimental Procedure 24

2.4 Purge Gas Egress-flow Measurement 24

2.4.1 PIV Principle 25

2.4.2 System Components and Parameters 26

Page

2.4.3 Experimental Procedure and Processing.........................32

3 RESULTS AND DISCUSSION.. 41

3.1 Single Stage Configuration 41

3.1.1 Experimental Conditions 41

3.1.2 Mainstream Gas Ingestion Measurements......................45

3.1.3 Purge Gas Egress-flow Field 49

3.2 1.5-stage Configuration.. 56

3.2.1 Experimental Condition..56

3.2.2 Mainstream Gas Ingestion Measurements......................57

3.2.3 Purge Gas Egress-flow field 59

4 CONCLUDING REMARKS... 66

REFERENCES 69

APPENDIX

A IMAGE CORRECTION PROCEDURE.. 71

B SEED PARTICLE DYNAMICS 84

LIST OF TABLES

Table Page

2.1 Permissible inlet conditions of gases to be analysed (NDIR gas analyzer) 22

2.2 PIV system components....26

2.3 PIV imaging parameters 33

2.4 PIV timing parameters....37

2.5 PIV processing parameters 38

3.1 Experimental Conditions for Single stage turbine configuration 41

3.2 Experimental boundary conditions 42

3.3 Experimental Conditions for 1.5-stage turbine configuration 56

B.1 Seed particle slip-velocity.... 87

LIST OF FIGURES

Figure Page

1.1 Schematic diagram - gas turbine internal air system (Courtesy: The Jet Engine, 1986) 2

2.1 Axial flow-Turbine experimental facility 8

2.2 Schematic of ASU Turbine rig 8

2.3 Schematic diagram of the single-stage turbine configurations (C: Gas Concentration tap, P: time-average static pressure tap, T: Thermocouple); all dimensions are in mm 13

2.4 Diagram showing the blade and vane arrangement for the single-stage turbine configuration; All dimensions are in mm 14

2.5 Schematic diagram of the 1.5-stage turbine configuration (C: Gas Concentration tap, P: time-average static pressure tap, T: Thermocouple); all dimensions are in mm 16

2.6 The pressure measurement system 18

2.7 Schematic of static pressure tap on stator disk 19

2.8 Arrangement for main gas ingestion measurement for the single-stage turbine configurations 23

2.9 PIV system components 26

2.10 Timing diagram for the Model 630150 POWERVIEW 4M camera 30

2.11 Schematic of the turbine stages. The shaded yellow region is mapped by PIV and the overlaid green squares represent the FOV. All the dimensions are in mm. 35

Figure Page

2.12 Light ray refraction through the outer shroud Plexiglass..........................35

2.13 Relative positions of vanes and blades for the PIV experiments. 36

2.14 Flowchart of Image processing steps in INSIGHT 6.1.............................38

3.1 Circumferential distribution of time-average static pressure at the outer shroud, stator rim seal and stator near its rim – $Re_{vax} = 1.14\times10^5$, $Re_\Phi = 5.86\times10^5$, $c_w = 1653$ for Configuration – I rim seal geometry..................44

3.2 Effect of cw on the radial distribution of time-average static pressure in the disk cavity at the stator disk- $Re_{vax} = 1.14\times10^5$, $Re_\Phi = 5.86\times10^5$, for Configuration – I rim seal geometry. 44

3.3 The radial distribution of sealing effectiveness at the stator disk surface for Configuration – I rim seal geometry for different experimental conditions..47

3.4 The radial distribution of sealing effectiveness at the stator disk surface for Configuration – II rim seal geometry for different experimental conditions..47

3.5 Comparison of the radial distribution of sealing effectiveness at the stator disk surface for Configuration – I & II rim seal geometries – Experimental Set - I 48

3.6 Comparison of the radial distribution of sealing effectiveness at the stator disk surface for Configuration – I & II rim seal geometries – Experimental Set – II 48

Figure Page

3.7 Comparison of the sealing effectiveness distribution within the rim-cavity at r/b = 0.9048, Configuration – I & II rim seal geometries – c_w=1653...49

3.8 Ensemble-averaged egress gas velocity vector map for $Re_{vax} = 9.32\times10^4$, $Re_\Phi = 4.63\times10^5$, $c_w = 1653$, for Configuration – I rim seal geometry at 1/3rd vane pitch location (dT = 2.0 μs)....................50

3.9 Ensemble-averaged egress gas velocity vector map for $Re_{vax} = 9.32\times10^4$, $Re_\Phi = 4.63\times10^5$, $c_w = 3226$, for Configuration – I rim seal geometry at 1/3rd vane pitch location (dT = 2.0 μs)....................51

3.10 Ensemble-averaged egress gas velocity vector map for $Re_{vax} = 9.32\times10^4$, $Re_\Phi = 4.63\times10^5$, $c_w = 8735$, for Configuration – I rim seal geometry at 1/3rd vane pitch location (dT = 2.0 μs)....................52

3.11 Ensemble-averaged egress gas velocity vector map for $Re_{vax} = 1.14\times10^5$, $Re_\Phi = 5.86\times10^5$, $c_w = 1653$, for Configuration – I rim seal geometry at 1/3rd vane pitch location (dT = 1.6 μs)....................53

3.12 Ensemble-averaged egress gas velocity vector map for $Re_{vax} = 1.14\times10^5$, $Re_\Phi = 5.86\times10^5$, $c_w = 1653$, for Configuration – I rim seal geometry at **2/3rd** vane pitch location (dT = 1.6 μs)...................53

3.13 Ensemble-averaged egress gas velocity vector map for $Re_{vax} = 1.14\times10^5$, $Re_\Phi = 5.86\times10^5$, $c_w = 3226$, for Configuration – I rim seal geometry at 1/3rd vane pitch location (dT = 1.6 μs)....................54

Figure Page

3.14 Ensemble-averaged egress gas velocity vector map for $Re_{vax} = 1.14\times10^5$, $Re_\Phi = 5.86\times10^5$, $c_w = 3226$, for Configuration – I rim seal geometry at **2/3rd** vane pitch location (dT = 1.6 μs)...................54

3.15 Ensemble-averaged egress gas velocity vector map for $Re_{vax} = 1.14\times10^5$, $Re_\Phi = 5.86\times10^5$, $c_w = 3226$, for Configuration – II rim seal geometry at 1/3rd vane pitch location (dT = 1.6 μs)....................55

3.16 Radial distribution of sealing effectiveness within the aft disk cavity, at the stator surface for Expt Set - III..58

3.17 Radial distribution of sealing effectiveness within the aft disk cavity, at the stator surface for Expt Set - IV 58

3.18 Circumferential variation of sealing effectiveness at the stator surface, at r/b = 1.0126 for Expt Set – III 59

3.19 Ensemble-averaged egress gas velocity vector map for $Re_{vax} = 6.67\times10^4$, $Re_\Phi = 4.93\times10^5$, $c_w = 1643$, at 1/3rd aft vane pitch location (dT = 3.0 μs) 60

3.20 Ensemble-averaged egress gas velocity vector map for $Re_{vax} = 6.67\times10^4$, $Re_\Phi = 4.93\times10^5$, $c_w = 3287$, at 1/3rd aft vane pitch location (dT = 3.0 μs) 60

3.21 Ensemble-averaged egress gas velocity vector map for $Re_{vax} = 7.12\times10^4$, $Re_\Phi = 5.26\times10^5$, $c_w = 1643$, at 1/3rd aft vane pitch location (dT = 3.0 μs) 61

Figure Page

3.22 Ensemble-averaged egress gas velocity vector map for $Re_{vax} = 7.12\times10^4$, $Re_\Phi = 5.26\times10^5$, $c_w = 3287$, at 1/3rd aft vane pitch location (dT = 3.0 μs) 62

3.23 Comparison of average radial velocity (from ensemble-averaged plots) at the 1/3rd vane pitch location, for different mainstream gas mass flow rate. 63

3.24 Ensemble-averaged egress gas velocity vector map for $Re_{vax} = 6.67\times10^4$, $Re_\Phi = 4.93\times10^5$, $c_w = 1643$, at the aft vane leading edge location (dT = 3.0 μs) 64

3.25 Ensemble-averaged egress gas velocity vector map for $Re_{vax} = 6.67\times10^4$, $Re_\Phi = 4.93\times10^5$, $c_w = 3287$, at the aft vane leading edge location (dT = 3.0 μs) 65

A.1 Light ray refraction through the outer shroud Plexiglass 72

A.2 Co-ordinate system for image correction. 73

A.3 A pictorial representation of generation of corrected image. The red labels (A&C) are corresponding to the labeling followed in Fig A.1 80

A. 4 Image of a Target 81

A. 5 Intensity histogram for one pixel row for Fig A.4 82

A.6 Image plane shift calculated from the refraction mapping procedure and measured from the validation image. 83

NOMENCLATURE

b	outer radius of disk cavity
C	tracer (CO_2) gas concentration
C_{vax}	vane axial chord length
c_w	non-dimensional mass flow rate of purge gas, = $\frac{\dot{m}_{purge}}{\mu b}$
$c_{w,fd}$	nondimensional free disk pumping flow rate, = $0.219 Re_{\Phi}^{0.8}$
dT, ΔT	laser pulse separation time
$\dot{m}_{purge}$	mass flow rate of purge gas (kg/s)
p	instantaneous static gage pressure
$\bar{p}$	time-average static gage pressure
p_{amb}	ambient pressure
$\underline{r}$	radial coordinate
Re_{vax}	main gas flow Reynolds number, = $\rho V_{ax} C_{vax} / \mu$
Re_{Φ}	disk rotational Reynolds number, = $\rho \Omega b^2 / \mu$
s	axial gap between rotor and stator disks
V_{ax}	mixed-mean axial velocity of main gas in annulus
β_2	angle, to axial direction downstream, of the main gas velocity relative to the blade – at just downstream of vane trailing edge (^{o})
ΔX	Displacement of tracer particle in the local x-direction of the Field of view

ΔY	Displacement of tracer particle in the local y-direction of the Field of view
η	local sealing effectiveness
μ	dynamic viscosity (kg/m/s)
ρ	density of gas (kg/m^3)
Ω	rotor disk speed
Φ	azimuthal coordinate.

Chapter 1

INTRODUCTION

1.1 Background

Efficient performance of gas turbine engines depends on the turbine rotor inlet temperature which has, over the years, steadily increased from 900 K to around 1800 K. Such high inlet temperatures, which are well above the melting temperatures of the airfoil materials, are viable mainly because of advancements in the cooling and sealing technologies.

Figure 1.1 shows the schematic of a gas turbine internal cooling/sealing air system and the mainstream hot gas flow path. The higher pressure in the main gas path leads to the transport of hot main gas into rotor-stator cavities (this is termed ‘ingestion’). This leads to overheating and consequent thermal fatigue of the cavity internals and especially of the rotor disk, thus affecting their durability. Main gas ingestion is typically countered by providing seals on the stator and rotor disk rims and by injecting lower temperature air (purge gas) bled from the compressor discharge into the cavities; this helps to cool the cavity internals and in purging the cavities.

The performance of a gas turbine is affected by, among other things, the magnitude of main gas ingestion, purge air flow rate, and the interaction of purge gas with main gas in the main gas path. Of importance is the configuration of the seals provided on the stator and rotor disk rims. Understanding the influence of rim seal configuration on main gas ingestion and purge gas egress flow field becomes crucial. Accordingly, in this work, three different rim seal configurations have been studied in model axial-flow air turbines.

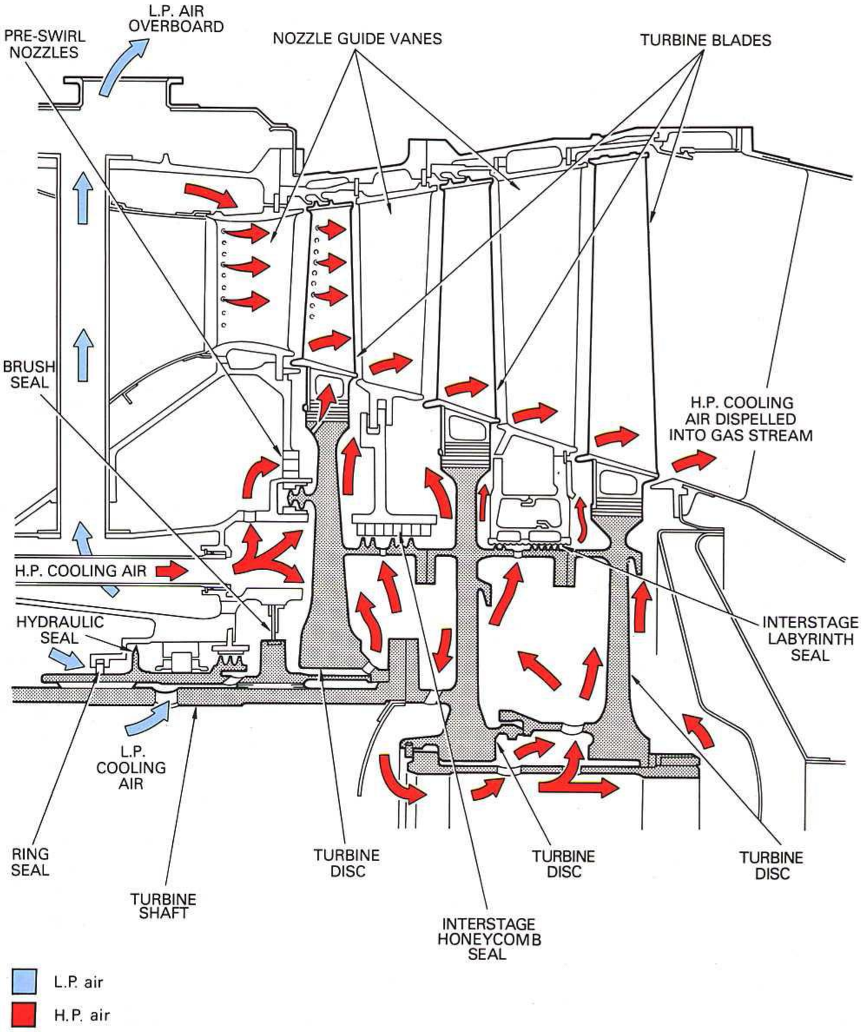

Fig 1.1 Schematic diagram - gas turbine internal air system (Courtesy: The Jet Engine, 1986)

1.2 Literature Survey

Many theoretical, computational and experimental studies have been performed to understand the mechanism of mainstream gas ingestion and the complex flow pattern. A brief discussion of selected works is presented in this section.

Phadke and Owen (1988 a,b,c) conducted a series of experiments – flow visualization, measurement of pressure and tracer gas concentration for different seal geometries to understand the main stream gas ingestion and the complex flow field. Three different external conditions viz, quiescent environment, quasi-axisymmetric external flow and nonaxisymmetric external flow were studied. The minimum purge gas flow rate $c_{w,min}$ required to prevent ingestion was estimated using the three different methods mentioned above. The circumferential pressure asymmetry in the main stream gas path was found to affect the minimum purge gas flow required to seal the cavity. This work is also discussed in Owen and Rogers (1989) which also provides a comprehensive detail of works undertaken previously to describe the ingestion of mainstream gas into disk cavities.

Green and Turner (1994) reported measurements of pressure and sealing effectiveness in a model turbine rig with guide vanes and rotor blades and a simple axial clearance seal. Tracer gas concentration measurements were carried out to determine the sealing effectiveness. They noted that ingestion in the presence of both vanes and blades tended to be lesser than that in the presence of vanes alone. The rotor blades seemed to make the mainstream gas flow more axi-symmetric and thus reduce ingestion

Johnson et al. (1994) identified the physical mechanisms inherent in the ingestion process. They noted that understanding of time-dependent three dimensional periodic pressure fields in the mainstream gas path and the turbulent mass transport in the rim seal region to be of paramount importance in gas turbine design.

Roy et al. (1999, 2000, 2005 and 2007) performed experiments on a model single-stage axial turbine stage with blades, vanes, and rim seals on the stator and rotor. Both unsteady and time-averaged static pressures were measured at various locations in the disk cavity and the main stream gas path. Tracer gas technique was employed to measure ingestion of mainstream gas within the disk cavity. Particle image velocimetry was carried out to study the flow within the disk cavity.

Gallier et al. (2000) employed particle image velocimetry and mapped the instantaneous velocity field in an axial-radial plane encompassing the main stream gas path and the rim seal region. The effect of rotor potential and the purge gas flow on the ingestion, egress and purge flow structure in the mainstream gas path were found to be significant.

McLean et al. (2001) conducted experiments to study the influence of coolant injection on the performance of gas turbine. Five hole pitot and Kiel probes were used to measure the rotor exit flow field. The purge gas was found to modify the rotor end-wall boundary layer and secondary flow development, thus modifying the turbine exit conditions.

Gentilhomme et al. (2002) conducted experimental, theoretical and numerical work on a single-stage axial turbine rig. Time average pressure distribution and ingestion were measured. Unsteady and steady CFD simulations were performed from which the unsteady effects due to the rotor were found to be an important parameter for ingestion.

Cao et al. (2003) carried out experimental and computational study of the interaction between the mainstream gas path flow and sealing air flow. Experiments were carried out in a two-stage axial turbine rig featuring a simple axial gap between the rotor and stator disks, without any rim seals. Fast response pressure transducers were installed in the disk space to measure the unsteady pressure. A 3-D unsteady simulation of the flow (without the vanes and blades) was carried out. Alternate regions of ingress and egress, which rotated at 90-97% of rotor speed, were found near the cavity rim.

Jakoby et al. (2004) reported a full 360º azimuthal domain simulation of time-dependent flow field on a 1.5-stage experimental turbine. Multiple low pressure regions that rotated at 80% of the local rotor speed were found to be present in the rim cavity. Mainstream gas ingestion was observed to occur in these regions.

Paniagua et al (2004) reported experimental and CFD results of a transonic HP turbine stage. Fast response pressure sensors were mounted on blades and platform to measure time-resolved static pressure. Five-hole pitot probe was used to map the flow field downstream of the turbine stage.

Zhou et al. (2009) reported experimental and CFD results of a model axial flow turbine stage with vanes, blades and rim seals. Three rim cavity configurations with different aspect ratio were studied. Tracer gas technique was used to measure ingestion of mainstream gas and PIV was employed to measure flow field within the cavity. Multiple regions of ingestion and egress were identified near the rim seal region of the cavity.

1.3 Overview of the Present Work

In this work, experiments were carried out in model single-stage and 1.5-stage axial-flow air turbines with blades, vanes and rim seals on both the stator and rotor. Though simpler than an actual gas turbine, the model turbines retained important features that influence main gas ingestion. Three different rim seal configurations were studied to understand their influence on ingestion and the interaction of purge gas with the main gas in the main gas path.

The thesis has been organized as follows.

- Chapter 2 provides description of the experimental facility, turbine stages, rim seal configurations, experimental techniques and procedures followed for measuring the quantities of interest
- Chapter 3 contains the experimental results and their discussion
- Finally, Chapter 4 presents the concluding remarks.

Chapter 2

TEST FACILITY AND EXPERIMENTS

2.1 Experimental Facility

Figure (2.1 and 2.2) shows the experimental facility that was used for the current work. The major components - the main blower, secondary blower and the rotor are described below.

Main Blower

The air flow required for the experiments is provided by a centrifugal blower (22.4 kW, Hauck, TBA-20-30) which is hereby referred to as the Main Blower. The main blower, controlled by a variable-frequency motor drive (Cutler-Hammer, AF 95), is capable of providing air flow rates of up to 1.42 m^3/s (≅ 3000 cfm). The rotor stage is placed on the suction side of the blower. The blower inlet is connected to a 292 mm (11.5”) i.d. plexiglass circular duct via a diffuser with a divergence angle of 5°. The blower discharges air to the ambient through an approximately 2235 mm (88.0”) long, 311 mm (12.25”) i.d. vertical pipe that is connected to an exhaust duct.

Measurement of the Mainstream Air flow Rate

A pitot tube rake (United Sensor, USNH-N-107), equipped with five pitot tubes spaced equally along a manifold is used to measure the mainstream gas flow rate, This is installed in the 292 mm i.d. plexiglass circular duct at approximately 984 mm (38.75”) upstream of the main blower inlet.

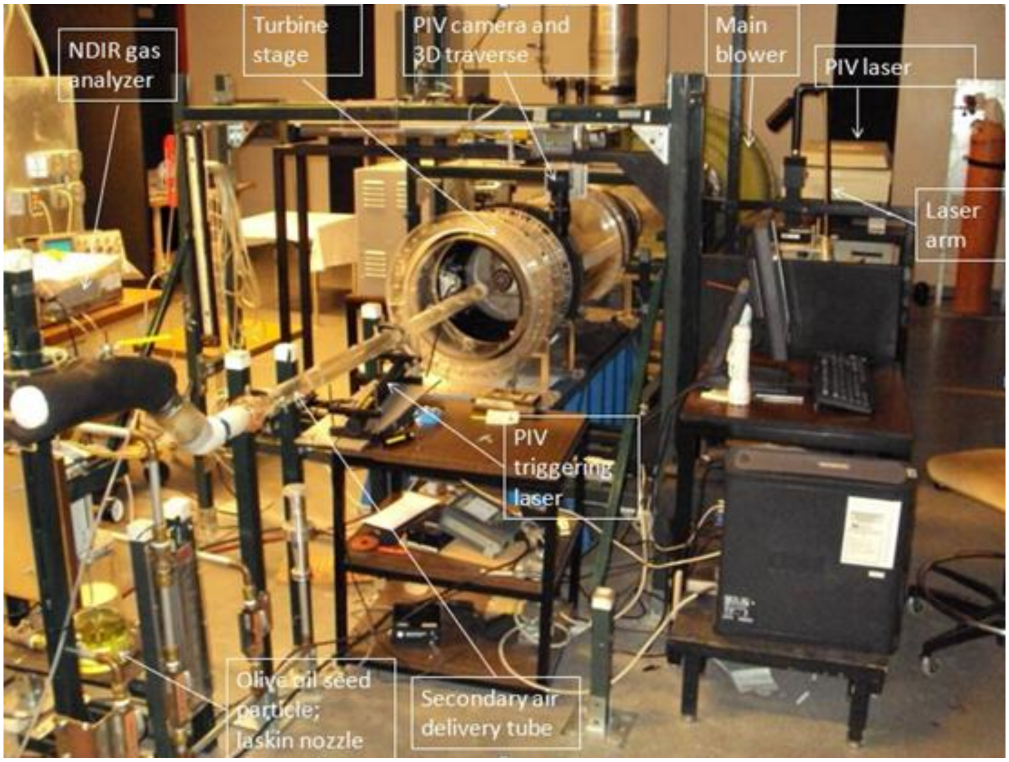

Fig 2.1 Axial flow-Turbine experimental facility

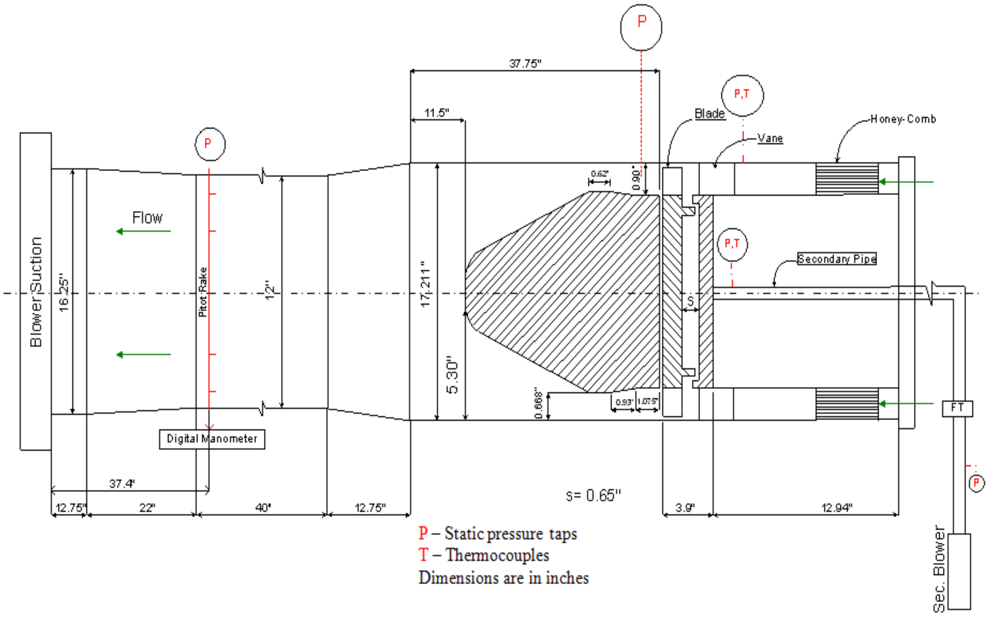

P – Static pressure taps
T – Thermocouples
Dimensions are in inches

Fig 2.2 Schematic of ASU Turbine rig

The Pitot tube rake is connected to a digital manometer (Validyne, PS309, range: 0-2” water gage) which measures the dynamic pressure head. The digital manometer provides an analog output (0-2V), which is routed to a data acquisition system (Analogic DATA 6500). The data acquisition system displays the mean and RMS values of the dynamic pressure head that are used to monitor the flow rate.

Secondary Blower

The Purge gas is supplied by another smaller centrifugal blower (2.24 kW, Hauck, TBA-16-3). The secondary blower, controlled by a variable-frequency motor drive (Emerson, Prism), is capable of providing air flow rates of up to 0.12 m^3/s (≅ 250 cfm). The secondary blower discharges air through a 50.8 mm (2.0”) nominal diameter insulated galvanized iron pipe equipped with a turbine flow meter. A 760 mm (29.9”) long pipe section is provided upstream of the flow meter to ensure a well developed flow. Additionally, a check valve is provided to regulate the flow.

Measurement of the purge gas flow rate

The purge gas flow rate is measured by a turbine flow meter (EG&G Flow Technology, FT-32). The flow meter indicator provides an analog output signal which is routed to a digital multimeter (Model 45, Fluke). A known calibration is used to convert the measured output voltage to the corresponding flow rate.

Rotor Drive

The rotor disks for all the different turbine stage configurations were mounted on a 50.8 mm (2.0”) diameter mild-steel shaft. The shaft is belt-driven by a motor; 2.24 kW (3HP, 1750 rpm max. GE). The speed of the motor is controlled through a 3.73kW adjustable-frequency drive (5 HP, Eaton-Cutler

Hammer). The belt-drive is a step up drive, with a speed ratio of 3.27:1, which allows a maximum rotor speed of 5722 rpm. The rotor speed is measured by a digital photoelectric tachometer (Biddle Instruments; Accuracy ±1 rpm). The AFD helps in maintaining the speed of the rotor at a constant value. The AFD is additionally equipped with a dynamic braking resistor (Power Ohm Resistors, P13549-405; rated at 2.8 kW at a total resistance of 65.0Ω) which enables a quick shut-down of the motor.

2.1.1 Turbine Stages

In this work, experiments were conducted on model single-stage and 1.5-stage turbines. Both turbine stages had similar inlet sections. A 120.7 mm (4.75") long honeycomb section (Polypropylene, 0.315" cell size, black, Plascore, PP30-5) is provided in the annular passage (Fig 2.2) at 152.4 mm (6.0") upstream of the vane leading edge to straighten the incoming mainstream gas flow.

2.1.1.1 The single-stage turbines

Figure 2.3 shows the schematic of the two different rim seal configurations that were used for the single-stage turbine. The mid-span shapes of the vanes and blades are also shown in Fig 2.4. For both the configurations, the axial gap (s) (between the stator and rotor disks) was maintained at 16.5 mm. An inner stator seal (at r= 153.2 mm), with an axial clearance of 2.5 mm with the rotor, was present in both configurations. This essentially divides the disk cavity into an inboard region called as 'Inner-cavity' and a radially outboard region called as 'Rim-Cavity' as shown in Fig (2.3). The only difference between the two configurations is in their stator & rotor rim seal geometries. One of them

(Configuration – I / Config - I) contains rim seals that have an axial overlap of 2 mm (0.08”) and a radial clearance of 2 mm (0.08”). The other configuration (Configuration – II / Config - II) features stator and rotor rim seals with an angular clearance (2 mm clearance), subtending an angle of 119.7° to the stator surface (Fig 2.3 b).

The turbine stage is located on the suction side of the blower. The 391 mm diameter, 31.8 mm thick aluminium rotor disk (present down-stream of the stator) has 28 partial-length and partial-height blades. The radial clearance between the blade tip and the steel shroud is 1.5 mm (0.059”). The plexiglass stator disk is 19.1 mm (0.75”) thick and has the same diameter as the rotor. There are 22 partial-height vanes which turn the incoming air by 68.6°, thereby imparting a realistic swirl to the air flow. The blade and vane heights are such that given the main blower capacity, sufficiently high main air stream-wise velocity can be obtained so as to result in an acceptable velocity triangle upstream of the blade row at prescribed rotor speeds. The purge gas is injected axially into the disk cavity at the stator hub by a 1780 mm (70.1”) long, 38.1 mm (1.5”) i.d. plexiglass tube.

Figure (2.4b) shows the velocity triangle diagram for the mainstream gas at the vane exit. β_2 is the angle (with respect to the axial direction), of the mainstream gas velocity (W_2) relative to the blade. A large positive value of β_2 ensures that the rotor operates as a turbine. Maintaining low rotor speeds and high mainstream gas flow rate would ensure a large positive value of β_2.

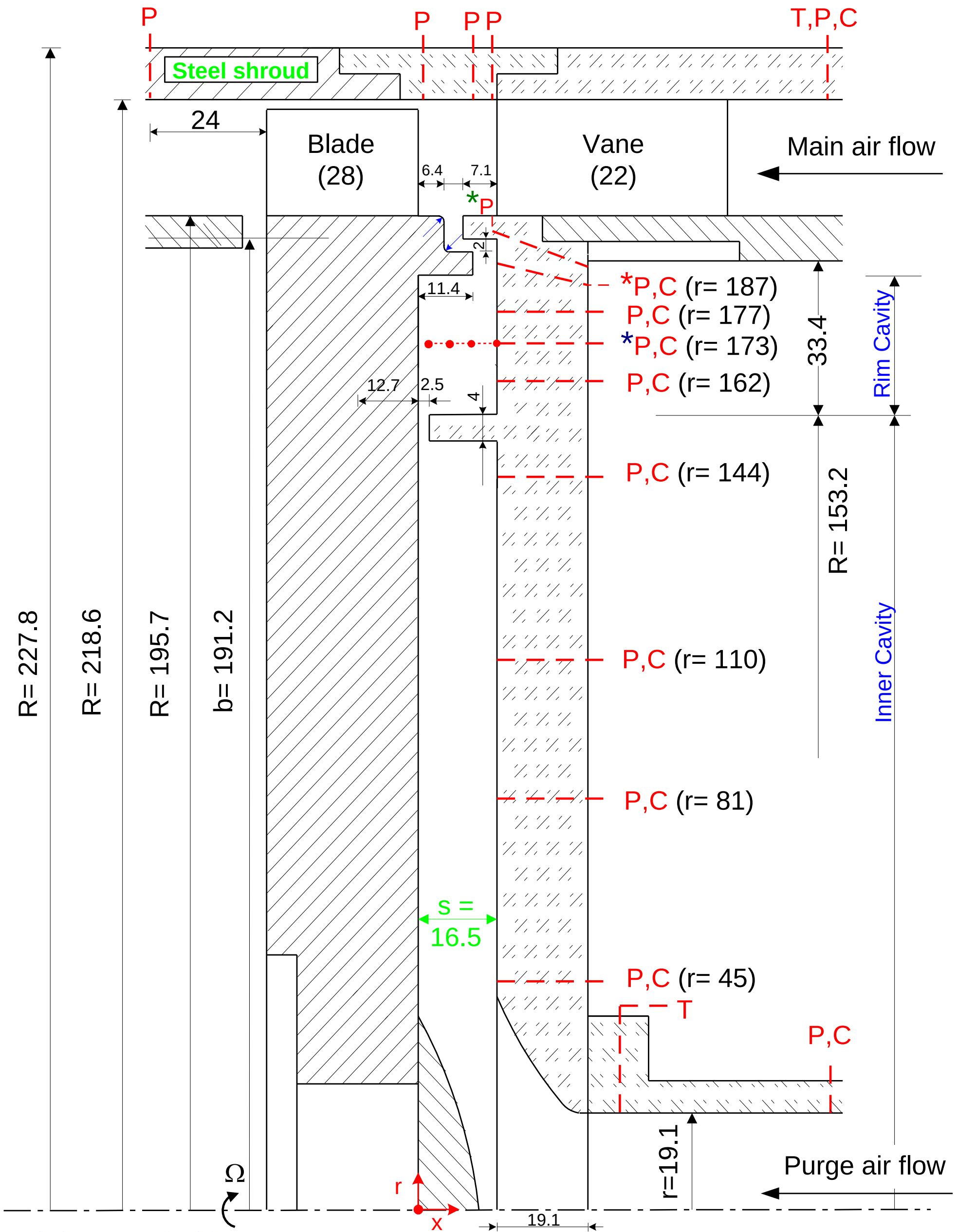

For both corners, radius (R)= 1 mm

* Circumferentially 17 locations over one vane pitch; * Circumferentially 16 locations over one vane pitch;

*Circumferentially 6 locations over one vane pitch

(a) Configuration – I rim seal geometry

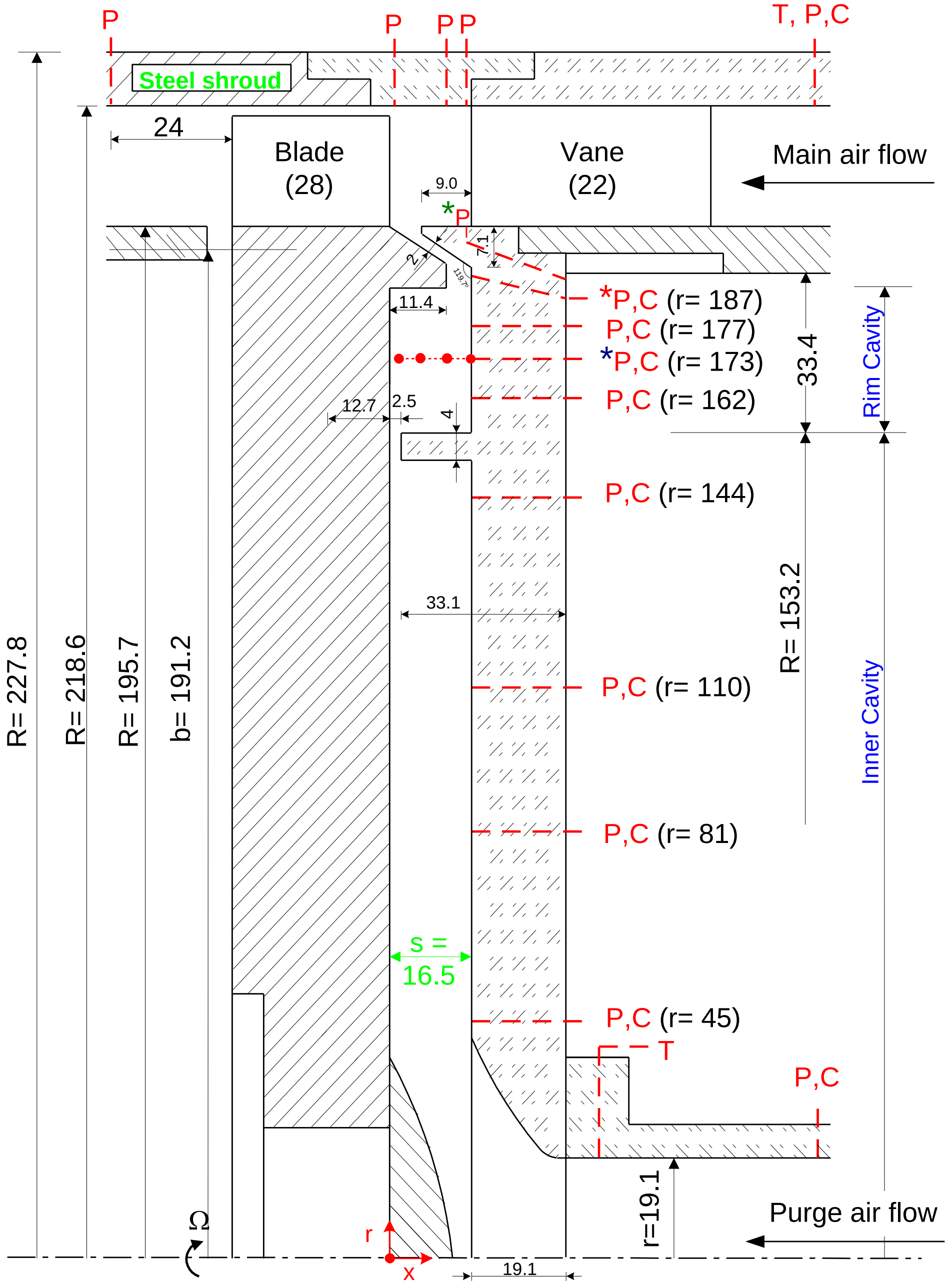

* Circumferentially 17 locations over one vane pitch; * Circumferentially 16 locations over one vane pitch;

*Circumferentially 6 locations over one vane pitch

(b) Configuration – II rim seal geometry

Fig 2.3 Schematic diagram of the single-stage turbine configurations (C: Gas Concentration tap, P: time-average static pressure tap, T: Thermocouple); all dimensions are in mm

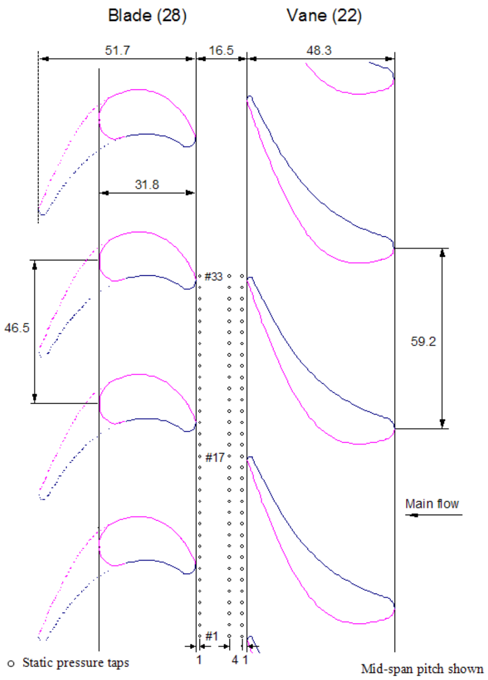

(a) Static pressure taps on outer shroud

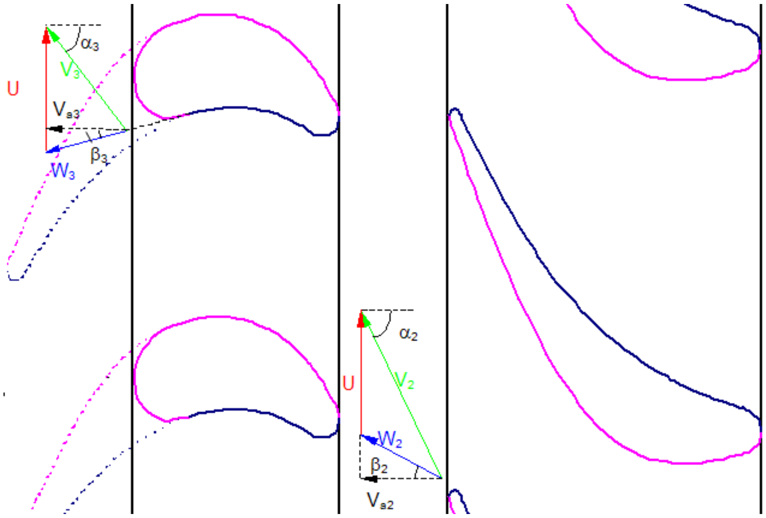

(b) Velocity triangle

Fig 2.4 Diagram showing the blade and vane arrangement for the single-stage turbine configuration; All dimensions are in mm

2.1.1.2 The 1.5-stage turbine

A schematic of the 1.5-stage turbine (vane-blade-vane) is shown in Fig (2.5). The 403.2 mm diameter (part plexiglass, part aluminium) rotor disk has 52 partial-height and partial-length blades. There are 59 partial-height and full-length vanes in the front and aft vane rows. The front vanes turn the incoming air by 60.1°. The purge gas is delivered to the aft disk cavity by a plexiglass tube which is connected to the rotating hub (as shown in the figure 2.5). The figure also shows the flow path of the purge gas. The aft disk cavity contains axially overlapping radial clearance rim seals on the stator and rotor (6.6 mm axial overlap and 2.6 mm radial clearance). Additionally, the aft disk cavity contains an inner labyrinth seal which divides the cavity into an inner-cavity and an outer (rim) cavity as shown in Fig 2.5.

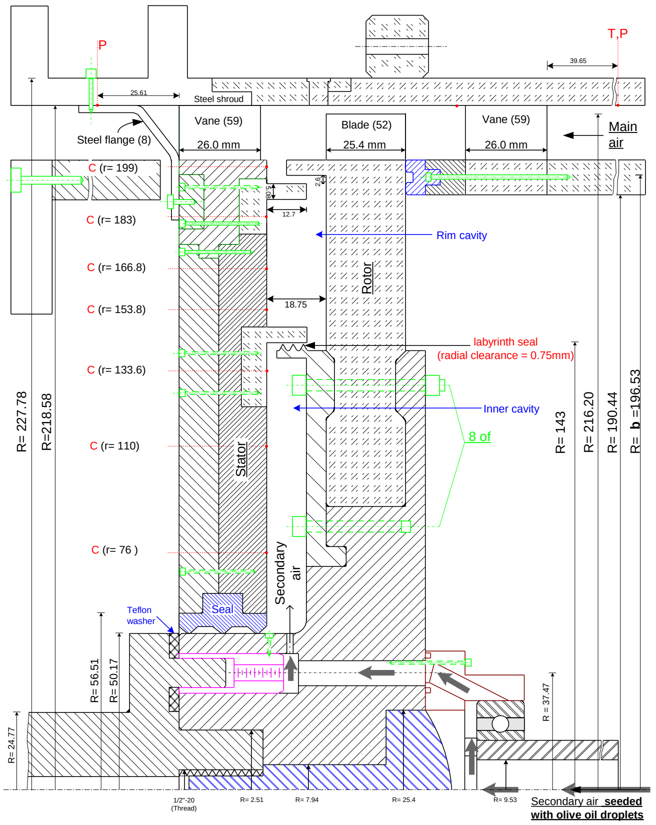

(a) 1.5-stage turbine configuration

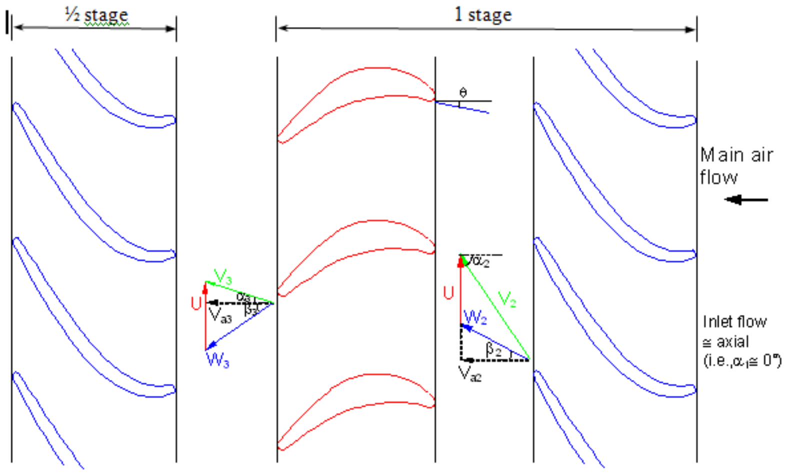

- α_3 is the 'swirl angle' for the gas velocity at blade exit.

- V is 'actual' air velocity.
- W is 'relative w.r.t. blade' air velocity.

(b) Blades – vanes arrangement and the velocity triangles

Fig 2.5 Schematic diagram of the 1.5-stage turbine configuration (C: Gas Concentration tap, P: time-average static pressure tap, T: Thermocouple); all dimensions are in mm

2.2 Time-Average Static Gage Pressure Measurement

For all the turbine stages presented here, initially, static gage pressure distributions in the mainstream gas path were measured to ensure that nominally steady flow had been achieved. The static gage pressure distributions were also measured within the disk cavity. In this section, a brief description of the experimental procedure and the instrumentation used for these measurements is presented. The static gage pressure measurement system consists of a Scanivalve, a differential pressure transducer and a signal carrier demodulator. The Fig (2.6) displays the different components of the system which are described briefly in the following section.

2.2.1 System Components

Scanivalve

Scanivalve is a device that contains 48 inlet channels and one outlet channel. To the inlet channels, Flexible vinyl tubes (VINL-063, Scanivalve Corp) connected to the pressure taps on the turbine rig, are connected. On manual operation, a solenoid-controlled stepper drive rotates the 48-channel fluid switch wafer such that, at any particular time, only one inlet is connected to the outlet. This helps in measuring the pressure from the different inlets sequentially. A binary encoder/decoder transmits the angular position of the scanivalve to a display system from which the channel information of the particular channel connected to the outlet could be read-off.

Pressure Transducer

A variable reluctance-type pressure transducer (DP-45 Validyne) with a range of 0-2 psi is used. The transducer contains two ports, one of which is connected to the Scanivalve outlet and the other is open to ambient air. Thus the transducer measures gage pressure. The transducer uses a sensing diaphragm which produces an output voltage corresponding to the applied pressure differential.

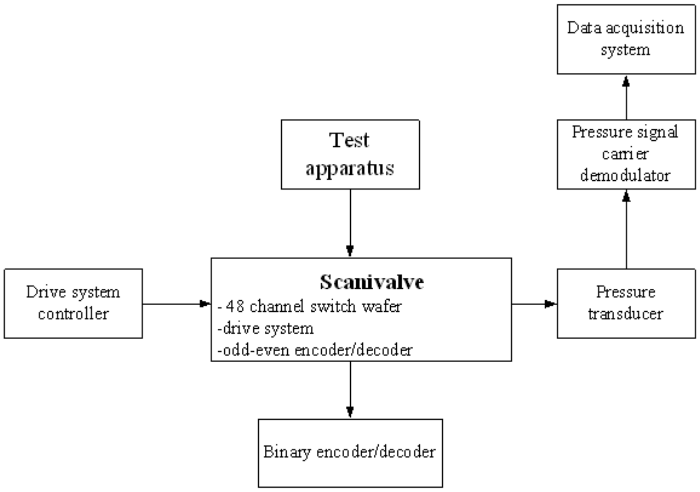

Fig 2.6 The pressure measurement system

Pressure Signal Carrier Demodulator

A pressure signal carrier demodulator (CD12, Validyne) provides excitation to DP45 pressure transducer and also acts as a signal conditioner. It has a high input sensitivity range (0.9 to 75 mV/V) which allows one to track even small fluctuation in the input signal in great detail. The output from the CD12 is displayed on the front panel (LED system) and is also routed to the data acquisition system.

Data Acquisition System

The output signal from the CD12 is routed to the data acquisition system 'Universal Waveform Analyzer (Analogic, DATA 6500)' which is programmed to display the time-mean and RMS values of the pressure signal over a sequence of 30720 data points with a sampling frequency of 500 μs.

Static pressure taps and their location

Figure (2.7) shows the design of a typical static pressure tap used in the measurements. Miniature bulged stainless steel tabulations (TUBN-063, 1.6 mm o.d, 1.0 mm i.d, Scanivalve corp) are used. It is ensured that no machining burrs are present near the pressure tap as they could affect flow conditions.

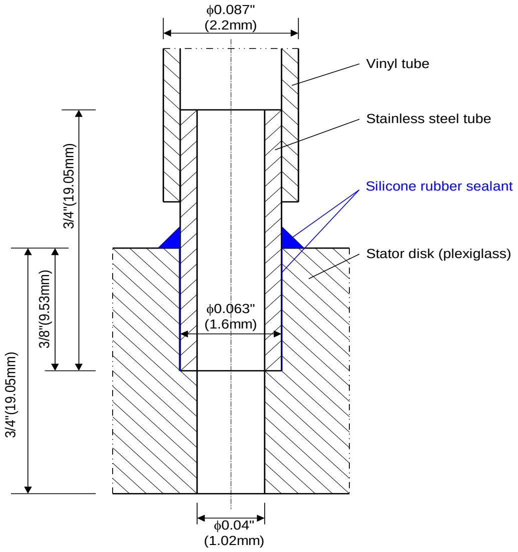

Fig 2.7 Schematic of static pressure tap on stator disk

Static pressure distributions were measured within the disk cavity and in the mainstream gas flow path. Consequently, pressure taps were placed at many locations as shown in Fig(2.3 and 2.4). To measure the radial distribution of static pressure at the stator disk, eight pressure taps (at r =45 mm, 81 mm, 110 mm, 144 mm, 162 mm, 173 mm, 177 mm and 187 mm) are placed along a radial line on the stator disk. Additionally, 16 pressure taps (at r = 187 mm) and 6 pressure taps (at r = 173 mm) are placed circumferentially over one vane pitch, to measure the circumferential distribution of static pressure on the stator disk within the rim cavity. To measure the static pressure distribution in the main gas path, 33 pressure taps, distributed over two vane pitches are placed on the outer shroud. Three such rows of pressure taps, placed at 1 mm, 5 mm and 15.5 mm downstream of the vane trailing edge (Fig 2.4), help in measuring the variation of the static pressure distribution in the main gas path between the vane trailing edge and blade leading edge. The static pressure distribution on the rim seal is measured using 17 pressure taps (distributed circumferentially over a vane pitch) placed on the stator rim seal surface facing the mainstream gas flow, at 1 mm downstream on the bane trailing edge plane.

2.2.2 Experimental Procedure

The main gas inlet and purge gas inlet pressures provide the boundary conditions for the experiments. These are respectively measured by pressure taps placed at, the outer-shroud, 20 mm upstream of the vane leading edge, and at the purge gas tube, 70 mm upstream of the cavity entrance (Fig 2.2). The different pressure taps (whose locations were discussed above) are connected to the Scanivalve by Flexible vinyl tubes (VINL-063, Scanivalve Corp). The Scanivalve sequentially connects the different pressure taps to the transducer for measuring the gage pressure. The measured gage pressure data are demodulated by the pressure signal carrier demodulator (CD 12), and the analog signal from the CD-

12 is routed to the Data acquisition system for providing the mean and RMS pressure values. The time-average static gage pressure is defined as

$$\bar{p} = \frac{1}{T}\int_0^T p(t)dt = \frac{1}{N}\sum_{i=1}^{N} p_i \qquad (2.1)$$

The data acquisition system was set to acquire 30720 points (N) at 2 kHz (500 μs sampling interval) to ensure that the fluctuations in the pressure readings arising out of blade passage are averaged out. The highest and lowest blade passage frequencies were, 0.887 kHz (1900 rpm) and 1.12 kHz (2400 rpm) for the experiments. The uncertainty in the time-average static gage pressure measurements was estimated to be ± 4%.

2.3 Mainstream Gas Ingestion Measurement

Tracer gas concentration measurements were employed to estimate the main gas ingestion into the disk cavity and thereby determine the effectiveness of the rim seal geometry. In this technique, the purge gas is seeded with a known volumetric concentration of the CO_2 tracer gas. Ingestion of main gas into the disk cavity reduces the concentration of CO_2 in the disk cavity fluid. The disk cavity fluid is sampled at various radial locations and the concentration of CO_2 (at those radial locations within the disk cavity on the stator surface) is measured using a gas analyzer. Using the concentration levels of CO_2, within and outside the stator-rotor cavity, one can compute the effectiveness of the rim seal.

2.3.1 System Components

NDIR Gas Analyzer

The ingestion measurement experiments require the use of a gas analyzer. In this work, NDIR (Non-dispersive Infra Red, Siemens-Ultramat 23) gas analyzer is used. This equipment estimates the concentration of a particular gas in a sample. The tracer gas (CO_2, one of the gases that the analyzer can trace) absorbs IR in a particular range of wavelength. By measuring the amount of radiation absorbed in that wavelength range; the concentration of CO_2 in the sample is estimated. The gas analyzer features an IR measuring cell, a safety filter, a sample gas pump and a flow meter. Sample gas inlet and exit, and the zero gas (N2) inlet ports are provided at the back. The table 2.1 provides the permissible range of different parameters at which the sample gases are analyzed.

Table 2.1 Permissible inlet conditions of gases to be analysed (NDIR gas analyzer)

Parameters of the sample to be analyzed	**Permissible range**
Inlet Pressure	0.5 to 1.5 bar (absolute)
Flow rate	1.1 to 2.0 (litre/minute)
Temperature	0 to 50^{o} C

The gas analyzer performs an auto-calibration (AUTOCAL) using the zero-gas (N_2) when turned on. This calibrates the zero and the sensitivity of the IR measuring cell. This calibration process can also be initiated manually by pressing the CAL key present on the analyzer keypad.

Gas Cylinders and Tube Connections

The set-up and tube connections for mainstream gas ingestion experiment are shown in Fig 2.8. Ultra high purity (99.99999% N_2) compressed nitrogen gas was used as the zero-gas for AUTOCAL. The purge gas was seeded with CO_2 approximately 1.7m upstream of the disk cavity entrance using a sparger tube (stainless steel, 6.3 mm o.d; 4.5 mm i.d) containing 15 holes (each of 1 mm diameter). The volumetric concentration of the CO_2 was maintained at a fixed value by controlling the CO_2 flow rate at the point of injection, using a pressure regulator (on the gas cylinder) and a needle valve. Two electric heaters as shown in the figure were used to maintain the temperature of the CO_2 gas at ambient temperature and prevent icing of the regulator by gas. A J-type thermocouple was used to measure the temperature of CO_2 which was displayed by a digital thermometer (Fluke 52 K/J thermometer).

Each concentration measurement (gas sampling) tap was connected to a separate toggle valve through vinyl tube (3/16” ID; 5/16” OD). All such toggle valves were connected in form of a manifold with a common outlet which enabled sampling the CO_2 gas concentration individually. A needle valve and a filter were connected to the outlet, from which a vinyl tube delivered the sample gas to the gas analyzer (through the back port).

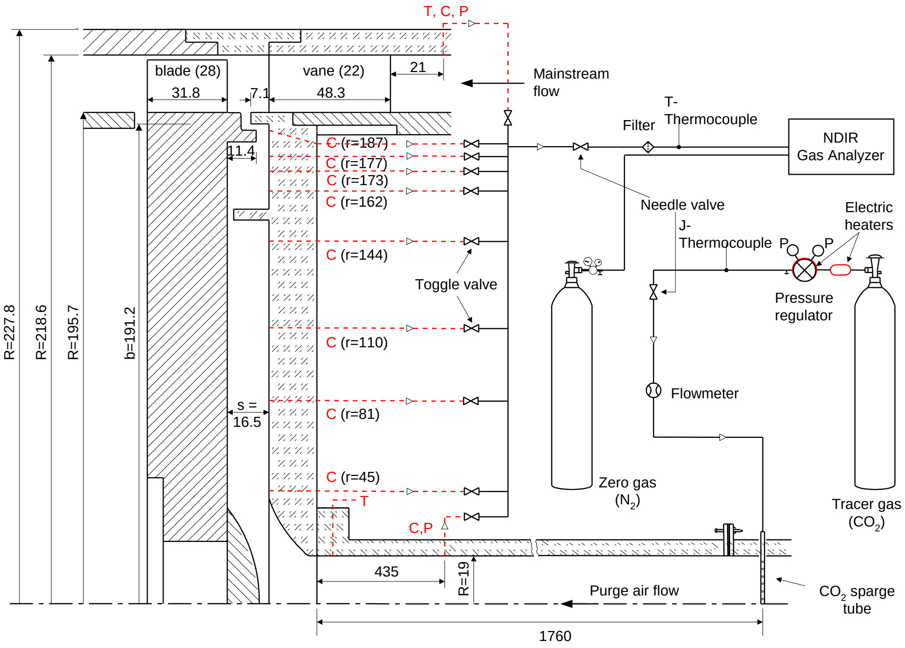

Fig 2.8 Arrangement for mainstream gas ingestion measurement for the single-stage turbine configurations

2.3.2 Experimental Procedure

As explained previously, a stainless steel tube (sparger) was used to seed the purge gas stream with a known volumetric concentration of CO_2. Another stainless tube (60 mm long, 5.5 mm o.d and 4.4 mm i.d), with 5 sampling holes (1mm dia each) spaced equally over a length of 35 mm was used to sample the tracer gas concentration in the purge gas at 0.435 m upstream of the purge gas entrance to the disk cavity. The CO_2 volumetric concentration at this location was maintained at 4.00 (± 0.11) percent. To serve as a reference value, the concentration of CO_2 in the main gas stream (lab ambient air) was also monitored during the experiments and was usually found to be 0.05 %. The taps as shown in Fig(2.3 and 2.5) at the eight radial locations (for single-stage configuration) and seven radial locations (for the 1.5-stage configuration) on the stator served as taps for measuring CO_2 concentration on the stator surface. Due to the nature of the measurements, the measured ingestion is a time-averaged value over many rotor revolutions, but is local with respect to the circumferential vane position and the radial location in the cavity.

2.4 Purge Gas Egress-flow Measurement

The purge gas egress flow field (in the main gas path) was measured using 2D - Particle image Velocimetry. This is a non-intrusive technique which allows spatially and temporally resolved mapping of instantaneous velocity field over a finite two dimensional plane at the same instant. This technique helps in identifying and visualizing flow structures in the region of interest.

2.4.1 PIV Principle

In this technique, the flow is uniformly seeded with light-scattering particles (called seed or tracer particles) that follow the flow faithfully. The region of interest (where one intends to make measurements) is illuminated using laser light (laser pulse) at *'two instances'* separated by a known time difference (ΔT or dT). The light scattered by the tracer particles (present in the region of interest) is captured by a high speed digital camera that records the *two instances* on separate frames using a CCD sensor present within the camera. The digitized images are stored in a computer for further evaluation. The displacements of the tracer particles (ΔX & ΔY) between the two laser pulses are estimated statistically from the stored images. The two images are divided into small sub-regions called interrogation spots, and each interrogation spot in the first image (also known as first frame) is cross-correlated with the corresponding spot in the second image (also known as second frame). The highest peak in the cross-correlation map (corresponding to a pair of interrogation spots) gives the mean displacement for that interrogation spot. This procedure is repeated until the displacement for all the interrogation spots is obtained. These measured Lagrangian particle displacements are then used to estimate the Eulerian velocity from the first order estimate of velocity as given below

$$U = \frac{\Delta X}{\Delta T} \tag{2.2a}$$

$$V = \frac{\Delta Y}{\Delta T} \tag{2.2b}$$

2.4.2 System Components and Parameters

The Fig(2.9) shows the PIV set-up used for the experiments. Any PIV system essentially consists of the components listed in Table 2.2 which are described below.

Table 2.2 PIV system components

Essential components of a PIV system	**Type of Component used in this work**
Light source	Dual cavity Nd-YAG laser (Spectra Physics PIV-200)
Light sheet optics	-200 mm Cylindrical lens; 700 mm spherical lens
Seed particle generation	Laskin nozzle particle generator (1-2μm dia Olive oil seed)
Recording device	4MP Power-view CCD camera (TSI)
Synchronizer	Model 610034, TSI
Image acquisition and processing	Insight 6.1 software

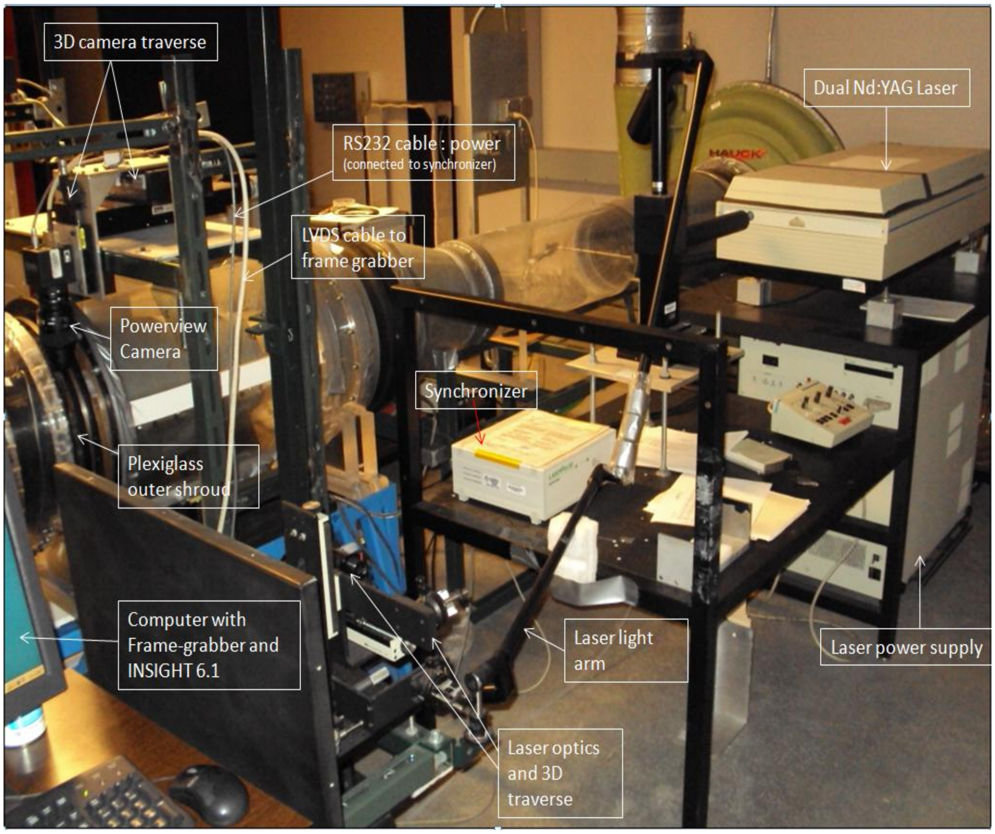

Fig 2.9 PIV system components

Light Source

Laser light is usually used for PIV experiments. Lasers have - high energy density, are monochromatic and can easily form thin light sheets. These characteristics of Lasers make them the most sought after Light source for PIV experiments. (Raffel 1998) gives a detailed account on the various types of lasers that can be used for a PIV measurement.

In this work, a dual cavity Nd-YAG (Spectra Physics PIV-200) laser was used. A harmonic generator (KD*P crystals) is used for doubling the frequency of the emitted laser i.e, the infra-red laser of 1064 nm wavelength is converted to visible green light of 532 nm wavelength. The laser was operated in the triggered mode using a Q-switch, which helped in obtaining short pulses (pulse-width of 10 ns) of high energy which is essential in PIV experiments (short pulse helps to avoid streaking of the particle images, and high energy helps in good scattering of light). An optimum Q-switch delay of 165 μs was used for the experiments. Subsequently pulses of 10 ns width with output energy of 247 mJ per pulse were obtained at a maximum repetition rate of 10 Hz. At this frequency, the two lasers had an average energy of 2.47 W.

Light Sheet Optics

The region of interest, (Field of view, FOV) is illuminated by a thin laser sheet (it should be a thin sheet, so that the illuminated volume can safely be approximated as a 2D plane). A particular combination of cylindrical and spherical lens (Table 2.2) was chosen to produce a laser sheet of 40 mm height and 1mm thickness (at the FOV) which ensured that the light sheet is of adequate intensity for illuminating the seed particles. A 3-D traverse was used to accurately position the laser light sheet at the required position. The traverse consists of right angled BK-7 prisms (to turn the incoming laser light) and lenses to generate the required laser sheet. The laser beam from the laser was delivered to the 3-D traverse by means of a light arm which houses specially coated mirrors and aluminium tubes (Fig (2.9)).

Seed Particle Generation and Supply

In PIV, velocity of the flow is indirectly measured from the velocity of the seeded tracer particles. This necessitates the tracer particles to faithfully follow the flow to achieve good accuracy in the velocity measurements. Particles present in a flowing fluid are subjected to drag forces that are proportional to their size. It is therefore important to have sufficiently small seed particle size so that the particle velocity does not lag the fluid velocity. Additionally, the light-scattering properties of the particle depend on its size (specifically - diameter, if spherical seed particles are assumed) where the intensity of scattered light is directly proportional to the particle diameter. Hence a trade off must be made to account for both particle lag and light-scattering. In this work, a Laskin nozzle particle generator (Raffel 1998) was used to generate olive oil droplets of size 1 µm -2 µm diameters. Compressed air of 7 to 7.5 psig pressure was used to atomize the olive oil and generate seed particles. The seed particles were injected into the purge gas stream, at approximately 1.8 m upstream of the disk cavity entrance.

Image recording

The PIV images were recorded using a high speed digital camera (4 Mega Pixel, PowerView, TSI). The camera housed a CCD sensor which contained a matrix of 2048×2048 light sensitive pixels (each pixel was 7.4µm × 7.4µm in size). A double frame/ single exposure method (also called as Frame straddling mode) was used to capture the images. In this mode of operation, the two images (arising from the two laser pulses) are captured on to separate frames and then cross-correlated to yield the velocity map.

In the frame straddling mode, the two images are captured on different frames. Usually, the time difference (ΔT / dT) between the laser-pulses is on the order of few micro-seconds and the image transfer time (from camera to computer) are much longer than this ΔT. So to enable the use of frame-straddling technique, the camera employed here featured a special type of CCD array called a – '**progressive scan interline transfer CCD array**' (details can be found in (Raffel 1998)). Here, adjacent to each active pixel, a masked (in-sensitive to light) storage site is present. After the first laser pulse, the active pixels rapidly dump the acquired charges of the first image into the adjacent storage site. The time taken for this is on the order of nano-seconds. This helps in preparing the sensor for the second image capture and also permits full electronic shuttering of the entire first image between the laser pulses. After the capture of the second image on to the active pixels, both the frames are read sequentially into the computer memory using an analog shift register. The Fig (2.10) displays the timing diagram for the camera used. The presence of masked storage region in the CCD camera reduces the light sensitive area of the sensor. To increase the percentage of available light sensitive area, micro-lenses are used which increase the fill ratio (percentage of available light sensitive area in a pixel) to 60%.

In the experiments, the images were captured at a frame pair rate of 3.33 Hz. This frame pair capture rate depends on factors such as frame rate of the camera (8.5 Hz or 4.25Hz frame pair rate), operating frequency of the laser (3.33 Hz), PCI bus limit of the frame grabber (120 MB/sec) and computer memory RAM (2 GB). Each image capture consists of two frames each of size 8 MB. With the above hardware settings, the maximum frame pair rate achievable is 3.33 Hz. (i.e, 3.33 image pair /s)

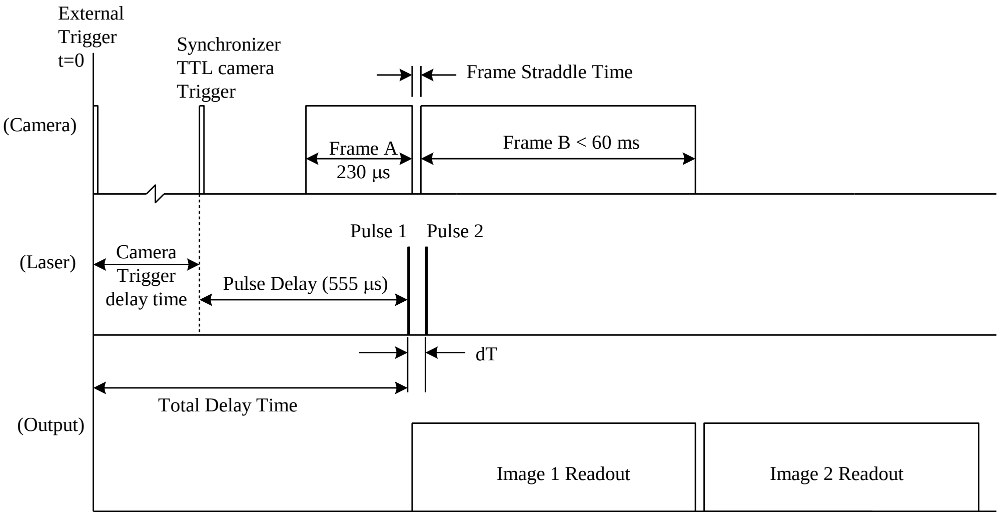

Fig 2.10 Timing diagram for the Model 630150 POWERVIEW 4M camera

Image Synchronization

The complete PIV experiment (image capture and laser firing) was software (Insight 6.1) controlled via a synchronizer (Model 610034, TSI). The Synchronizer was the timing module for the experiments. It was connected to the computer, frame grabber, camera, laser and the external trigger and synchronized the operation of all the components. The synchronizer was in turn controlled by the Insight software.

For experiments involving rotating machinery (i.e, with rotor and stator), measurements must be made at the same juxtaposition of the blades and vanes. To achieve this, the Synchronizer was triggered by an external TTL signal generated via a once-per revolution He-Ne laser pulse (details of which can be found in Ganesan 2007).

The Fig (2.10) shows the timing diagram of the camera and the laser pulses. The camera and laser pulse sequence begins immediately after the Synchronizer receives a signal from the external trigger. The **camera trigger delay time (CTD)** is the time from the initiation of the external trigger until the Synchronizer activates (triggers) the camera. This is an important parameter in measurements involving rotating machinery. As stated above, the CTD is adjusted appropriately to make measurements at the same relative positions of the blades and vanes. The time from the end of the first exposure to the start of the second is referred as **Frame Straddle time**. During this short time (which is in order of few hundred nano-seconds) the First image is transferred (dumped) into the adjacent storage sites, thus preparing the CCD arrays for the second exposure. Another important parameter is the **Pulse Delay** which is the time from the start of the camera trigger until the first laser pulse. In the frame-straddling mode, the pulse delay is the parameter that is adjusted to pulse the laser precisely towards the end of the first frame (A). Once the Synchronizer initiates a pulse sequence, it ignores all external trigger signals until the completion of that particular pulse sequence.

2.4.3 Experimental Procedure and Processing

Image Acquisition

In the present work, PIV was employed to map, in the radial-axial plane of the mainstream gas path, the purge gas egress flow in the region between the vane trailing edge plane and the blade leading edge plane. The laser light sheet was introduced radially inward through the polished plexiglass outer shroud, Figs (2.11 and 2.12). A 3-D traverse system (for laser optics) was used to precisely position the laser sheet at the desired location. To eliminate any reflection of the laser light, the blades and vanes were painted flat black as were appropriate surfaces of the rim seals; these are indicated by red lines in Fig (2.11). A 3-D traverse system (for the camera (Fig 2.9)) was set-up such that the camera, with its axis oriented perpendicular to the laser sheet, imaged the field of interest (FOV) denoted by green lines in Figs (2.11).

The projection of the FOV on the r-φ plane is the line AC in Fig (2.12). Since the camera imaged the FOV through the curved plexiglass outer shroud, Fig (2.12), the image as seen by the camera contained distortion due to light ray refraction. This distortion is along the radial co-ordinate (AC) only and is non-uniform because of varying shroud thickness that rays from different points on AC passed through. A mapping algorithm (Appendix A) similar to one developed in (Murphy 2009) was employed to correct each of the image prior to cross-correlation.

A 105 mm camera lens (Nikon Micro-Nikkor) was used for all the PIV experiments as it gave the optimum Field of view. Additionally to confer to the recommended rule of PIV (Adrian 1991) that the out-of-plane movement of the seed particles (within time dT) should be less than one-fourth of the laser sheet thickness, the time interval between the laser pulses (dT) was chosen to be on the order of few micro-seconds (1-3 μs). The shift in the vane-blade positions within this time interval was less than 0.04° in the azimuthal direction at the maximum rotor speed for the experiments. The table (2.3) gives typical values used in the experiments for the different Turbine configurations.

Table 2.3 PIV imaging parameters

Turbine Configuration	**Magnification**	**Field of view (mm × mm)**	**dT (μs)**
Single stage	0.705	21.5 × 21.5	1.6 to 2.0
1.5 stage	0.582	26.13 × 26.13	3.0

PIV measurements were obtained at the 1/3rd and 2/3rd vane pitch locations for the Single stage turbine configurations (Fig (2.13)) and at 1/3rd vane pitch & vane trailing edge locations for the 1.5 stage configuration. At each measurement location, five instantaneous images were obtained which were ensemble-averaged to obtain the mean velocity field.

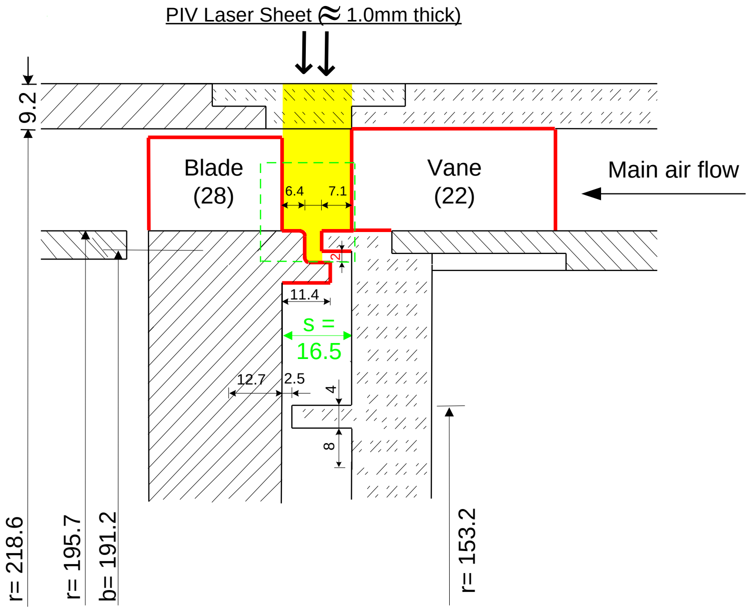

(a) Rim seal configuration – I

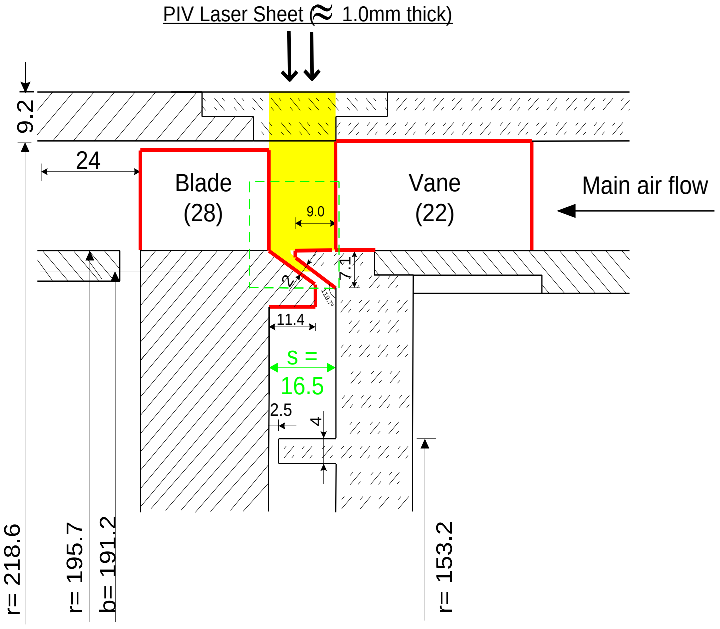

(b) Rim seal configuration – II

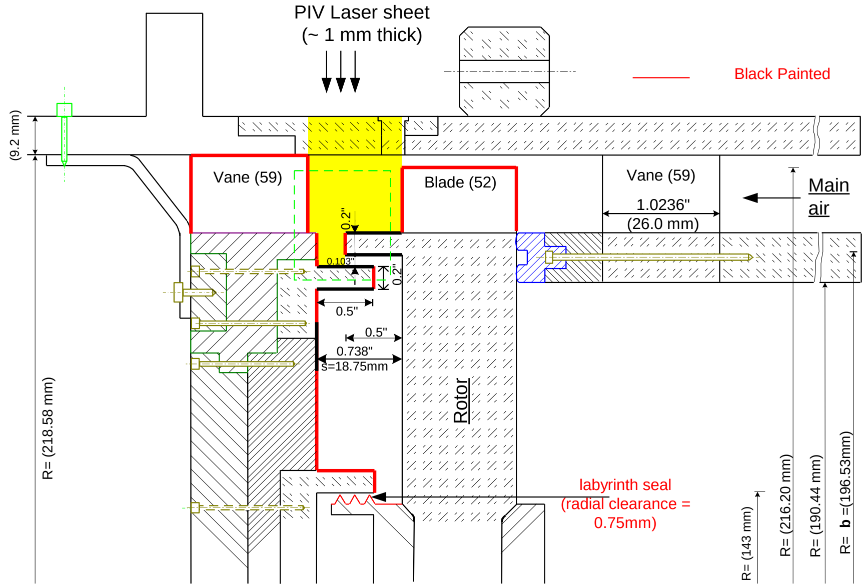

(c) Rim seal configuration – III (1.5 stage configuration)

Fig 2.11 Schematic of the turbine stages. The shaded yellow region is mapped by PIV and the overlaid green squares represent the FOV. All the dimensions are in mm.

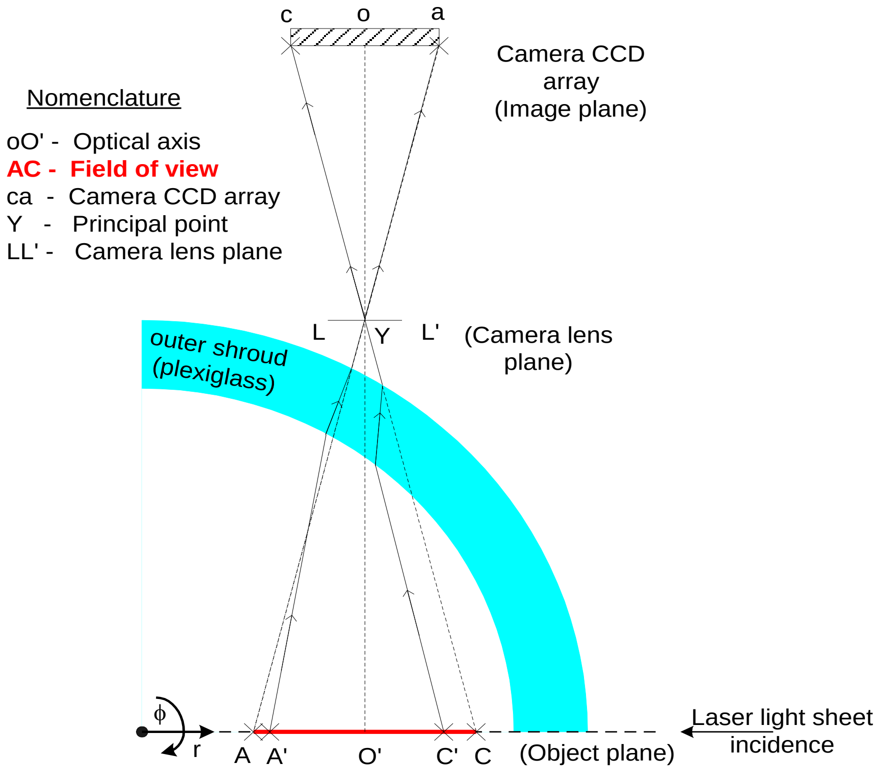

Fig 2.12 Light ray refraction through the outer shroud Plexiglass

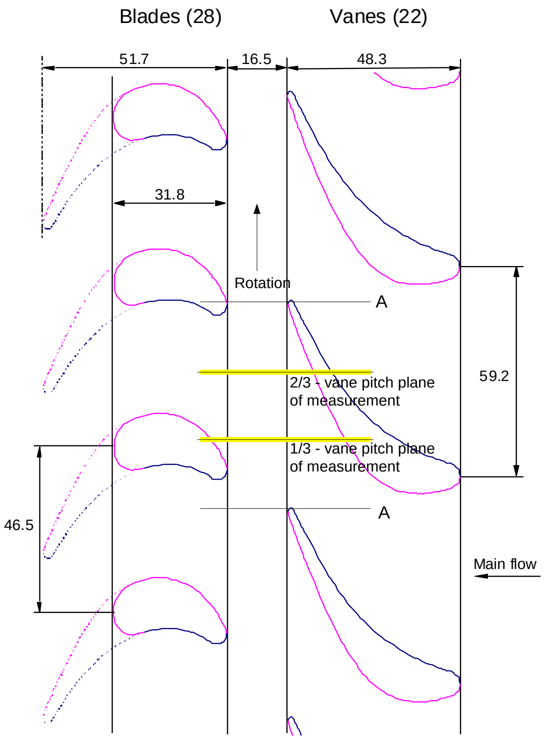

(a) Single-stage turbine configuration (For rim seal configurations I & II)

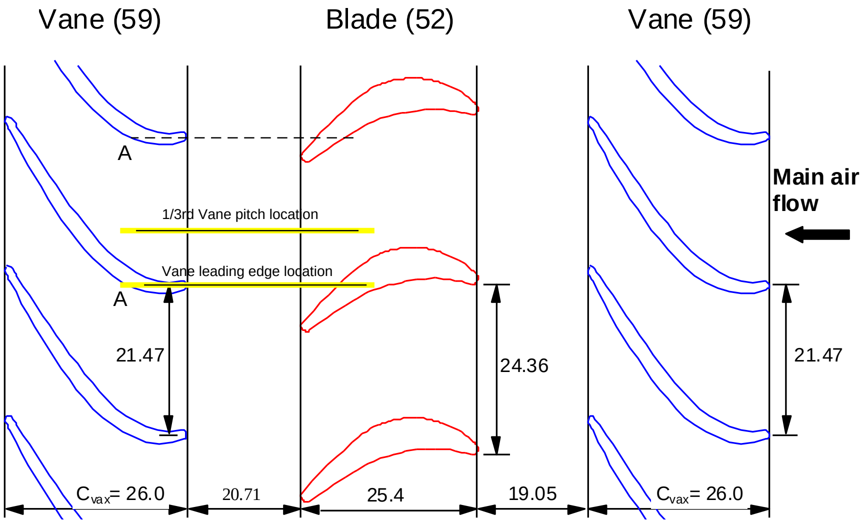

(b) 1.5-stage turbine configuration (For rim seal configuration – III)

Fig 2.13 Relative positions of vanes and blades for the PIV experiments.

The image acquisition was controlled by the software INSIGHT 6.1 (TSI Inc). It acts as the control module to co-ordinate image acquisition with the Synchronizer. User can specify different timing parameters to acquire the images. The Table (2.4) gives the typical values used for one of the experiments.

Table 2.4 PIV timing parameters

Parameters	**Single-stage**	**1.5-Stage**
Pulse separation time (dT) (μs)	2.0	3.0
Pulse pair repetition rate (Hz)	3.33	3.33
Pulse Delay time (ms)	0.555	0.555
Q-switch delay time (μs)	165	165
Camera trigger delay time (ms)	2.122	1.389
Number of image captures	5	5

Processing

Apart from image acquisition, INSIGHT is used for analysis and data validation also. The acquired images are initially corrected (using Matlab) for the distortion caused by light refraction by using the mapping procedure developed in Appendix-A. The corrected images are then cross-correlated using INSIGHT. The Fig (2.14) depicts the different processing steps carried out to obtain the final velocity vector field. The grid engine divides the images into small spots (interrogation spots) which are conditioned by the spot mask engine based on the requirements of the correlation engine. Next, the correlation engine computes the correlation function and returns the correlation map from which the maximum displacement peak is estimated by the peak engine. This process is repeated for all the interrogation spots. The vector field is then validated using different in-built validation filters and stored as a vector file. The table 2.5 lists the different parameters used in this work for PIV processing.

Table 2.5 PIV processing parameters

Parameters	Settings
Grid Engine	Recursive Nyquist Grid, with 50 % overlap, and spot size of 32 pix × 32 pix
Spot Mask Engine	No Mask used
Correlation engine	Hart Correlator
Peak Engine	Bilinear peak

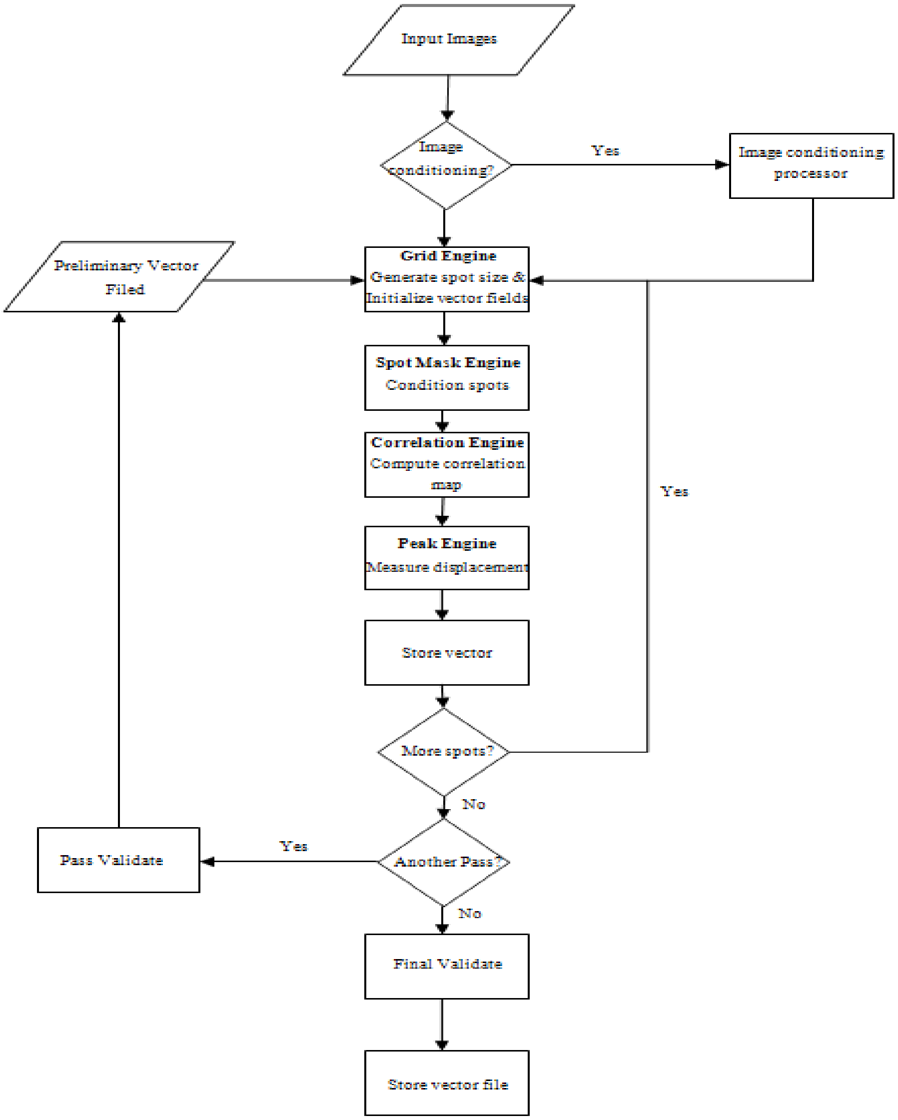

Fig 2.14 Flowchart of Image processing steps in INSIGHT 6.1

Grid Engine

‘Recursive Nyquist Grid’ was used for the experiments. This grid engine allows multiple passes to calculate the vector field. The multiple passes lend better accuracy in computing the vector field. In the initial pass the images are divided into interrogation spots (of size 32 pix × 32 pix) using which the vectors are computed. These results are used to optimize the spot offsets for the next pass. Additionally a 50 % overlap on the grid spacing was used which resulted in higher spatial resolution of the vectors in the vector field.

Spot Mask Engine

This parameter is usually used to condition an interrogation spot based on the requirements of the Correlation engine. Some correlation engines (like FFT correlator) work only with ‘square’ spot sizes. By using appropriate settings of this parameter, non-square spots are zero-padded to convert them into square spots. In this work, we used the Hart Correlator which works with non-square interrogation spots too. Hence, the ‘No Mask’ engine was used.

Correlation engine

Correlation engine computes the cross-correlation function for the two frames, and returns the correlation map. In this work, Hart Correlator was used for all the experiments. This correlation engine reduces sub-pixel bias errors and eliminates spurious vectors from the velocity field. It multiplies the correlation map of one interrogation spot with one or more neighboring spots. Any correlation peak that does not appear in both the correlation maps is eliminated. A correlation map, apart from the displacement peak, will contain other noise peaks.

The highest peak (corresponding to the displacement peak) from this map is obtained by the ‘Bilinear Peak Engine’

Validation

The estimated vector field usually contains many spurious vectors. Insight provides various inbuilt filters to eliminate these spurious vectors. In this work, validation filters like ‘standard deviation’, ‘median’, and ‘mean’ were used (details can be found in Raffel 1998). A MATLAB program was then used to convert the validated PIV vector fields from pixel co-ordinates to the real co-ordinates. The generated data file (real co-ordinates) was plotted using TECPLOT 8.0 to show the velocity vector map.

Chapter 3

RESULTS AND DISCUSSION

3.1 Single Stage Configuration

3.1.1 Experimental Conditions

Experiments were carried out for two different rotor speeds and mainstream stream gas flow rates as shown in Table (3.1). The conditions are specified in terms of non-dimensional parameters: Main gas flow Reynolds number (Re_{vax}), rotor disk rotational speed (Re_{φ}) and non-dimensional mass flow rate of purge gas (c_w). The rotor speeds and main gas flow rates were chosen such that β_2 was large and positive, which ensured that the rotor operated in the turbine mode. The purge gas flow rates were chosen with reference to the free-disk pumping flow rate (which is the pumping flow rate due to a flat disk rotating freely in a quiescent environment).

All the experiments viz., Time-average ingestion measurements and the purge gas egress flow PIV, were performed for all the experimental conditions specified in Table (3.1).

Table 3.1 Experimental Conditions for Single stage turbine configuration

Exp. Set No.	**Mainstream gas Flow rate (Re_{vax})**	**Rotor Speed (Re_{Φ})**	**β_2 (^{o})**	**Free Disk Pumping Flow rate ($c_{w,fd}$)**	**Purge gas Flow rate (c_w)**		**PIV vane pitch location**	
							1/3rd	**2/3rd**
I	9.32×10^4 ± 0.1×10^4	4.63×10^5 ± 0.005×10^5	49.7	7463	(a)	1653±79	measured	Not measured
					(b)	3226±79	measured	Not measured
					(c)	8735±79	measured	Not measured
II	1.14×10^5 ± 0.01×10^5	5.86×10^5 ± 0.005×10^5	48.3	9011	(a)	1653±79	measured	measured
					(b)	3226±79	measured	measured
					(c)	8735±79	measured	Not measured

Compared to Expt Set –I, the rotor speed was higher by 26 % and main stream gas flow rate was higher by 21 % for Expt set-II. Both the rotor speed and main gas flow rates were adjusted to maintain the value of β_2 in the main gas velocity triangle downstream of the vane trailing edge as close to equal as possible since velocity triangle influences the ingestion process (Roy et. Al 2005). This means that the effect of either the rotor speed or the mainstream gas flow rate on the time-average static pressure distribution, mainstream gas ingestion measurements could not be isolated.

Table 3.2 lists the values of the different boundary conditions used in the experiments. The values of the static pressure of mainstream gas at vane inlet and purge gas at cavity inlet changed slightly as the mainstream and purge gas flow rates were changed.

Table 3.2 Experimental boundary conditions

Parameters	Value
Average lab ambient pressure	97.5 kPa (absolute)
Average lab ambient temperature	23º C
Average static pressure of mainstream gas at vane inlet	96.0 kPa (absolute)
Average static pressure of purge gas at disk cavity entrance	93.0 kPa (absolute)

For all the rim configurations, initially, the static pressure measurements in the main gas path were carried out to ensure that nominally steady and circumferentially-periodic flow had been achieved. Subsequently, pressure distribution within the disk cavity was also measured. The pressure tap locations for the measurements are given in Section 2.2.1 and Fig (2.3 & 2.4). For brevity, the pressure measurements are reported only for Expt Set- II of Table 3.1.

The Fig (3.1) shows the static pressure distribution at the main gas path outer shroud for Experimental Set – II with c_w = 1653 for Configuration – I rim seal geometry. The static pressure in the main gas path outer shroud varies periodically with a period equaling the vane pitch. These measurements ensure that nominally steady and circumferentially- periodic flow are achieved. The peak pressure downstream of the vane trailing edge occurs in the mid-region of the vane wakes. The asymmetry in the mainstream gas path static pressure is highest at the 1mm downstream of the vane trailing edge location and gradually decreases downstream. The static pressure values on the stator rim seal and within the rim cavity are lower when compared to the mainstream gas path pressure values. The static pressure on the rim seal surface varies circumferentially whereas the static pressure within the disk cavity remains almost at a constant value circumferentially. Thus the pressure asymmetry caused by the vanes is dissipated across the rim seals. This pressure differential between the mainstream gas path at the vane rim-seal platform and the disk cavity could influence the ingestion of main gas into the rotor-stator cavity.

Figure (3.2) shows the radial distribution of static pressure on the stator disk of the Config – I rim seal geometry, within the disk cavity. As c_w is increased, the pressure level within the cavity increases.

From the cavity pressure distribution (Fig 3.2) it is seen that, the static pressure values on the stator, for lower c_w increases gradually along the radius.

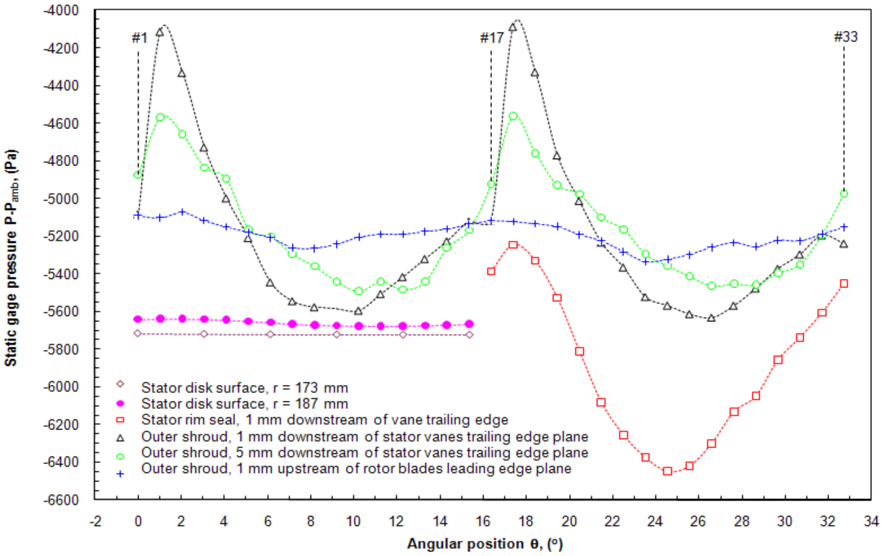

Fig 3.1 Circumferential distribution of time-average static pressure at the outer shroud, stator rim seal and stator near its rim – $Re_{vax} = 1.14\times10^5$, $Re_{\Phi} = 5.86\times10^5$, $c_w = 1653$ for Configuration – I rim seal geometry

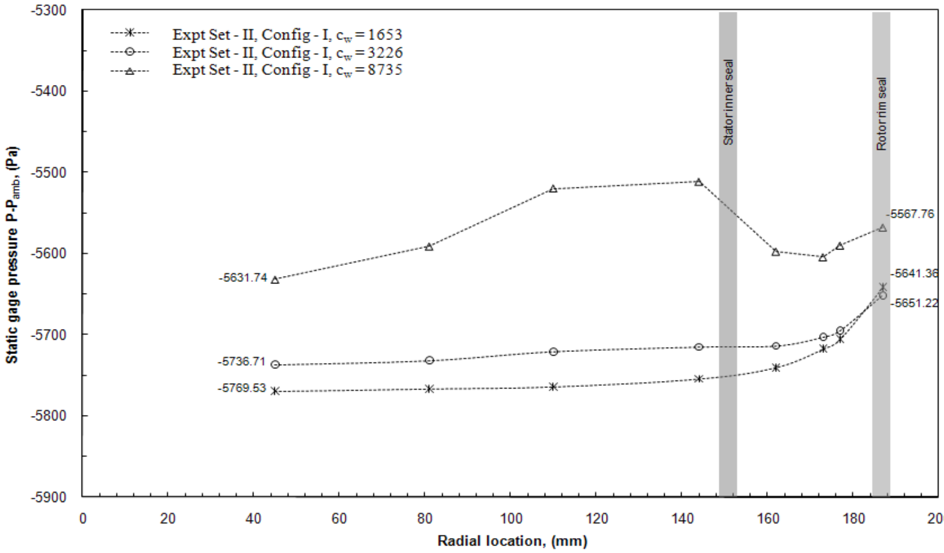

Fig 3.2 Effect of c_w on the radial distribution of time-average static pressure in the disk cavity at the stator disk- $Re_{vax} = 1.14\times10^5$, $Re_{\Phi} = 5.86\times10^5$, for Configuration – I rim seal geometry.

For the highest c_w case, the pressure value increases at a higher rate within the inner-cavity and drops across the stator inner seal. This trend in pressure value for the highest purge gas flow rate could be due to the blocking of the purge gas by the stator inner seal.

3.1.2 Mainstream Gas Ingestion Measurements

The main gas ingestion measurements in the disk cavity are expressed in terms of sealing effectiveness, which represent the combined effects of purge gas flow rate and rim seal geometry in effectively sealing the disk cavity from the main gas ingestion, and is defined as below

$$\eta(\underline{r}) = \frac{C(\underline{r}) - C_{main}}{C_{purge} - C_{main}} \tag{3.1}$$

The value of η ranges from 0 (no sealing) to 1.0 (perfect sealing).

Fig (3.3) shows the radial distribution of sealing effectiveness at the stator disk in the disk cavity for both the experiment Set I and II for Config - I. Increasing the rotor speed and the main gas flow rate (Expt Set II) decreases the sealing effectiveness (or increases the mainstream gas ingestion). This could be due to the combined effect of higher disk pumping and the higher peak to peak pressure value in the main gas path (at outer shroud) both of which influence main gas ingestion. From Fig (3.3), it is seen that the stator inner seal greatly reduces the main gas ingestion into the inner-cavity. For all purge gas flow rates (and for both experimental sets) the inner stator seal, seals the inner-cavity almost completely from mainstream gas ingestion (where $\eta = 0.9532$ is the least value at the minimal purge flow rate Fig(3.10)). Ingestion is mainly observed in the rim-cavity region. This could mean that, at low purge gas flow rate, the ingested mainstream gas is mostly confined within the rim-cavity and only a small amount of it gets ingested into the inner-cavity.

As the purge gas flow rate is increased, the sealing effectiveness goes up. Increasing the purge gas flow rate while maintaining constant main gas flow rate pressurizes the disk cavity (increases the static gage pressure as shown in Fig(3.2)), thereby reducing the pressure gradient between the disk cavity region and the main gas path which in turn reduces main gas ingestion (3.3). At purge gas flow rates closer to the free disk pumping flow rate, the value of sealing effectiveness approaches 1.0 at the stator.

Fig (3.4) shows the radial distribution of sealing effectiveness for the two experiment sets for Configuration – II rim seal geometry. The trends are similar to those of Configuration-I rim seal geometry. In Figs (3.5 & 3.6) the radial distributions of sealing effectiveness for the two different rim seal geometries (Config I &II) are compared. From these figures, it is seen that, in the inner-cavity, both the rim seal geometries perform almost equally well. There are small differences in the values of the sealing effectiveness in the inner-cavity region, between the two different rim seals. (the percentage change in η values between the two configurations, within the inner-cavity region is within 1 % (average)). Greater differences in the values of sealing effectiveness are found in the rim-cavity region. Hence, the stator inner seal shields the disk cavity from the influences of rim seal geometry differences.

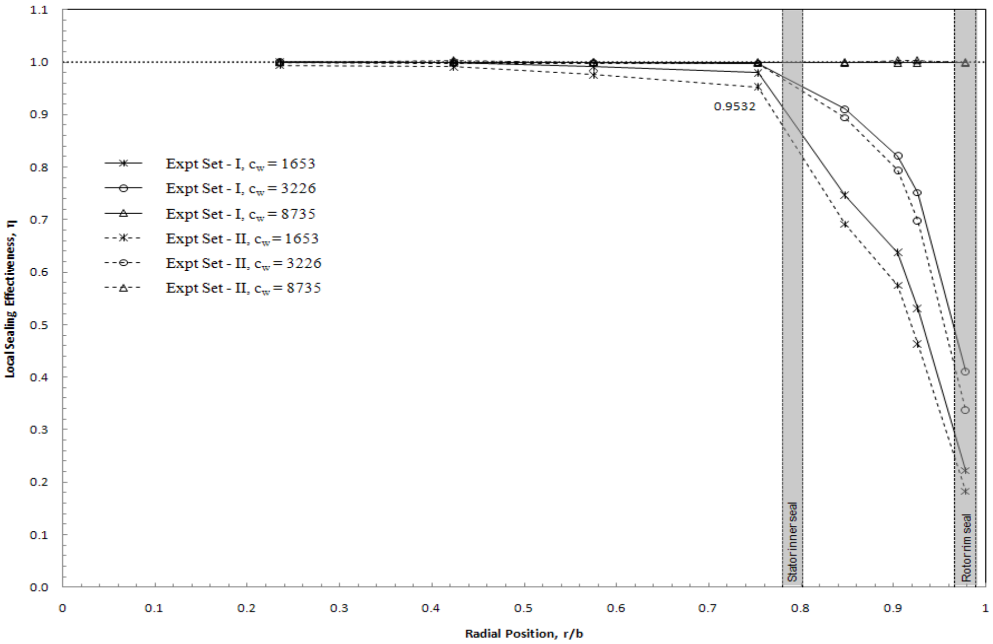

Fig 3.3 The radial distribution of sealing effectiveness at the stator disk surface for Configuration – I rim seal geometry for different experimental conditions

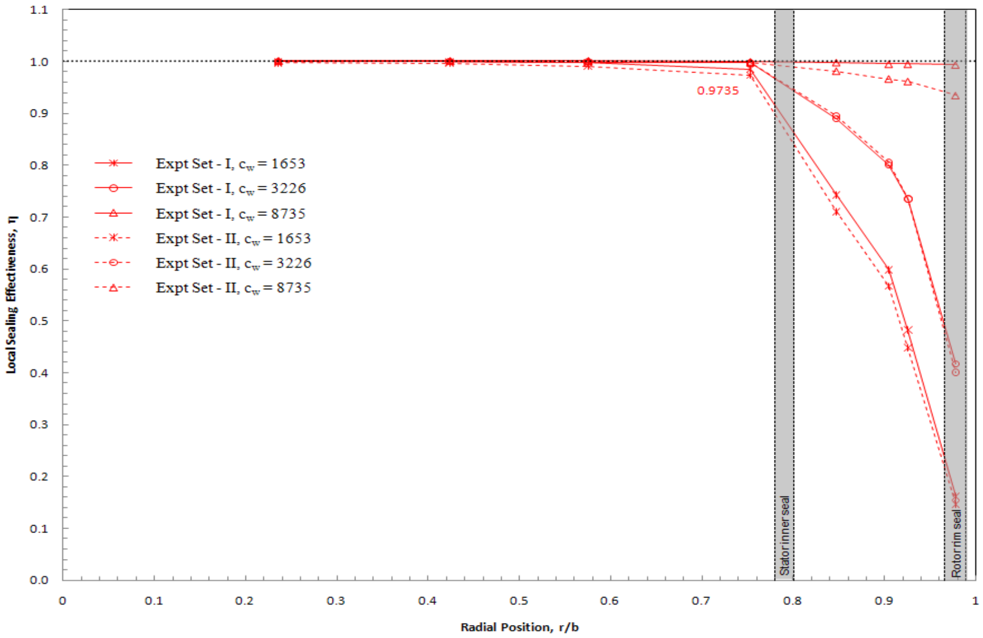

Fig 3.4 The radial distribution of sealing effectiveness at the stator disk surface for Configuration – II rim seal geometry for different experimental conditions

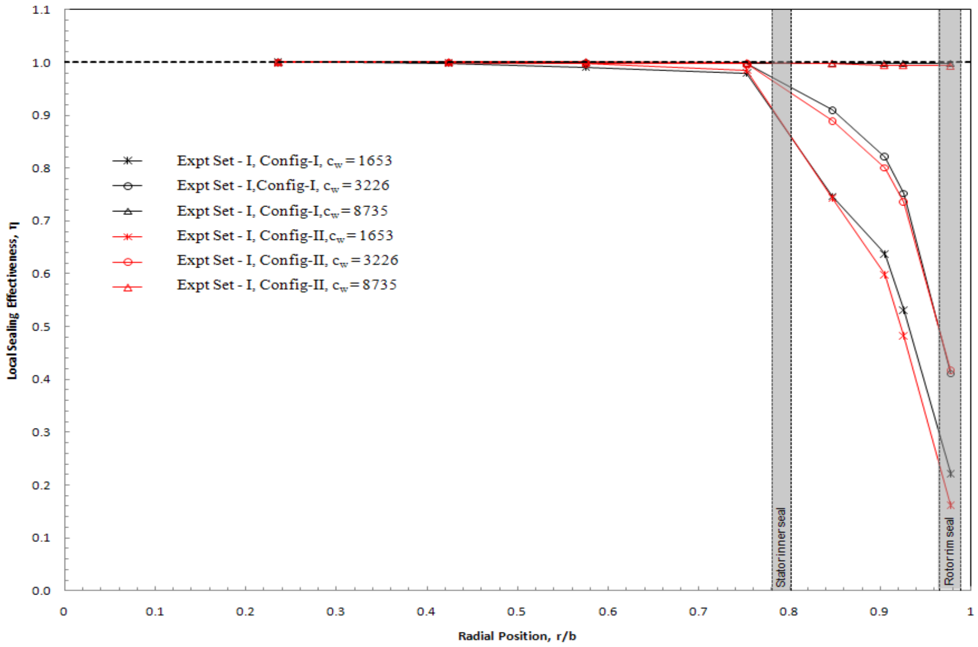

Fig 3.5 Comparison of the radial distribution of sealing effectiveness at the stator disk surface for Configuration – I & II rim seal geometries – Experimental Set - I

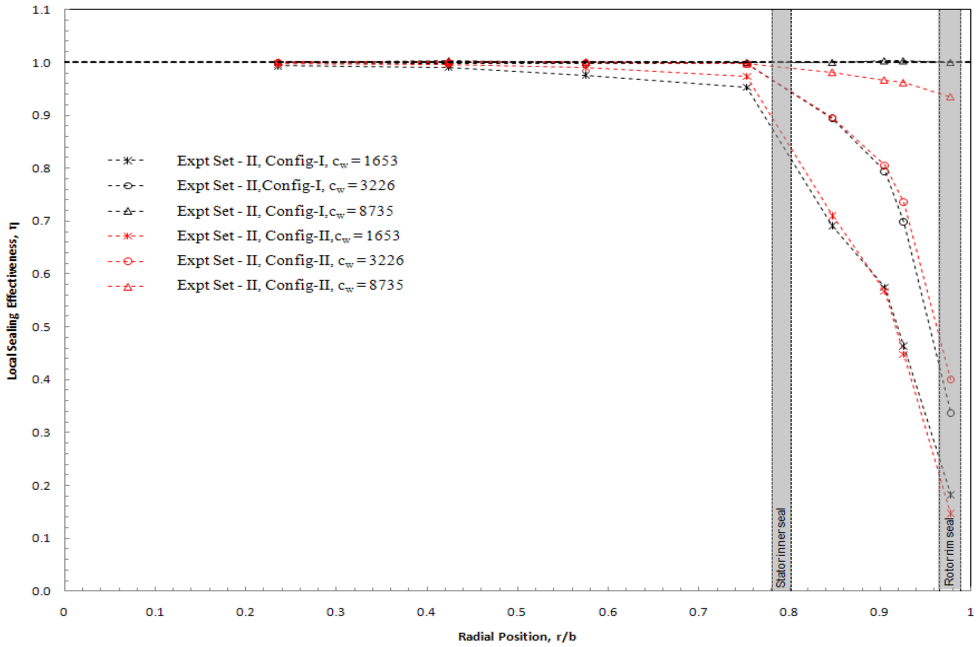

Fig 3.6 Comparison of the radial distribution of sealing effectiveness at the stator disk surface for Configuration – I & II rim seal geometries – Experimental Set – II

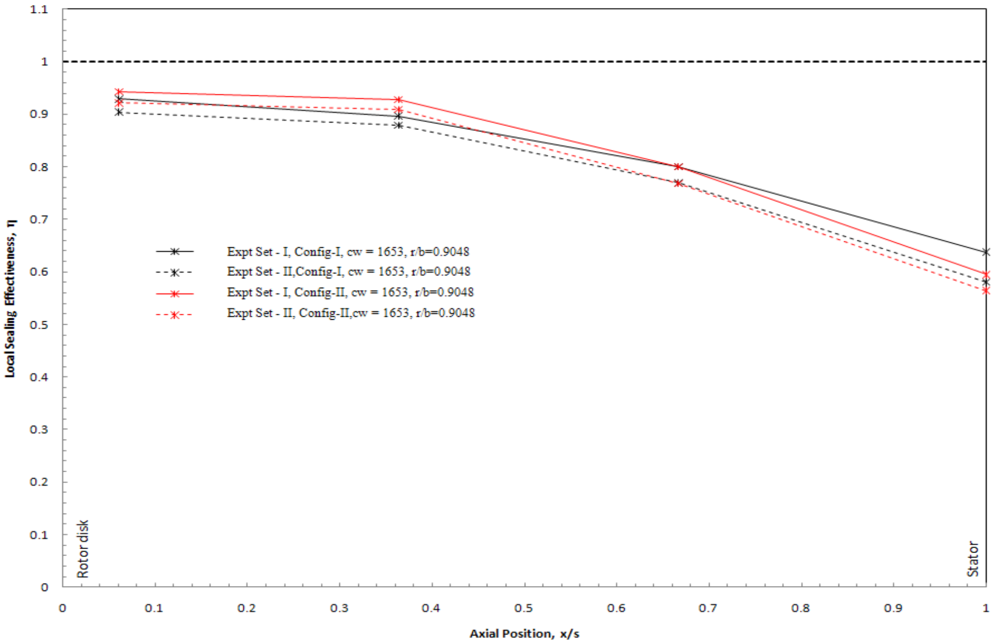

Fig 3.7 Comparison of the sealing effectiveness distribution within the rim-cavity at r/b = 0.9048, Configuration – I & II rim seal geometries – c_w=1653

Ingestion measurements were also performed within the disk cavity at different axial positions (x/s = 0.0606, 0.3636, 0.6666, 1; s=16.5 mm) at a particular radial location (r=173 mm; r/b = 0.9048) and purge gas flow rate (c_w= 1653). Measurements at the other radial locations and purge gas flow rates were not performed as the ingestion measurements within the disk cavity were time consuming. From figure (3.14) it is seen that irrespective of the experimental condition and rim seal configuration, the main stream gas ingestion is maximum at the stator disk and minimum near the rotor. This is due to the strong radial outflow of the purge gas near the rotor disk, which progressively impedes the ingested mains gas from reaching the rotor disk. This trend has been found in earlier works which featured similar rim seals (Roy et al 2000, 2001).

3.1.3 Purge Gas Egress-flow Field

Particle image velocimetry was employed to map, in the radial-axial plane of the mainstream gas path, the purge gas egress flow field in the region between the vane trailing edge plane and the blade leading edge plane. The velocity vector maps presented here are all ensemble-averaged maps. The ensemble averages were obtained from five instantaneous velocity vector maps.

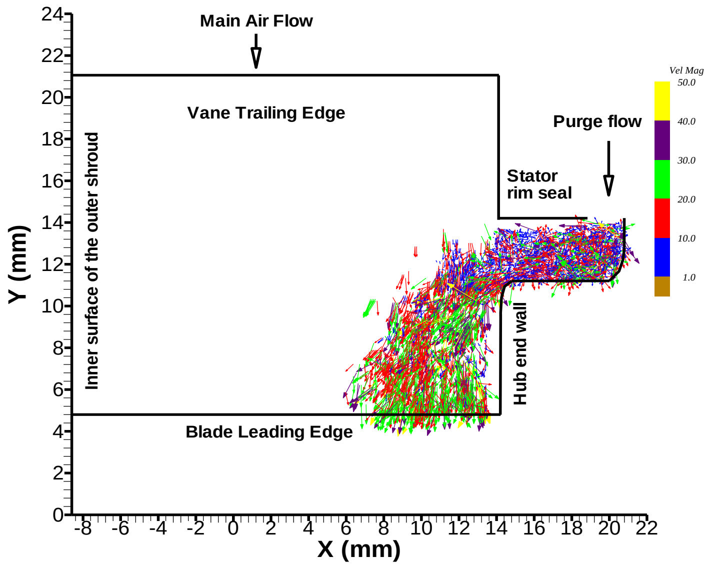

Fig 3.8 Ensemble-averaged egress gas velocity vector map for $Re_{vax} = 9.32\times10^4$, $Re_\Phi = 4.63\times10^5$, $c_w = 1653$, for Configuration – I rim seal geometry at 1/3rd vane pitch location (dT = 2.0 μs)

The egress flow field for Experimental Set – I for Configuration – I rim seal geometry has been plotted in Figs (3.8 – 3.10). From these plots, it is clear that the egressing purge gas will have significant influence on the main gas flow field, upstream of and in between the blades. This has implications for blade and end-wall cooling as well as aerodynamic loss.

As the purge gas mass flow rate is increased, there is a greater radial penetration of the purge gas into the main gas path. This is because; higher purge gas mass flow rates have higher radial momentum. At the highest purge gas flow rate, it was difficult to maintain sufficiently dense seeding of the purge gas, which resulted in the velocity vector maps to be sparse as seen in Fig (3.10)

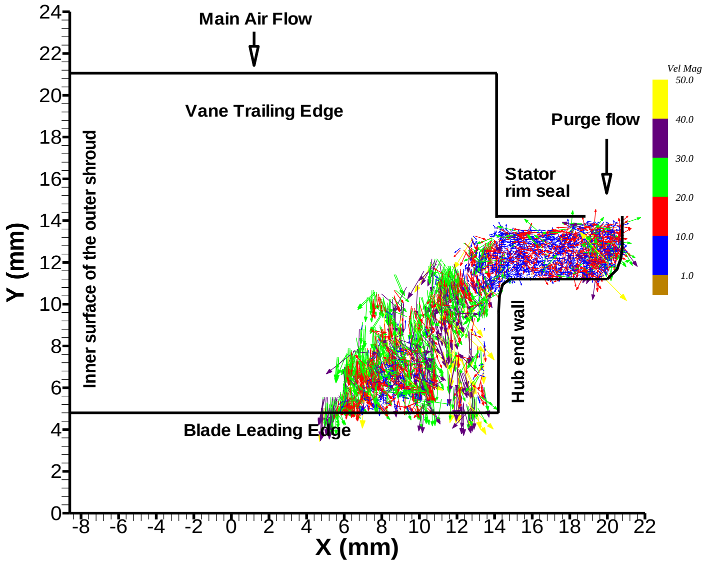

Fig 3.9 Ensemble-averaged egress gas velocity vector map for $Re_{vax} = 9.32\times10^4$, $Re_{\Phi} = 4.63\times10^5$, $c_w = 3226$, for Configuration – I rim seal geometry at 1/3rd vane pitch location (dT = 2.0 µs)

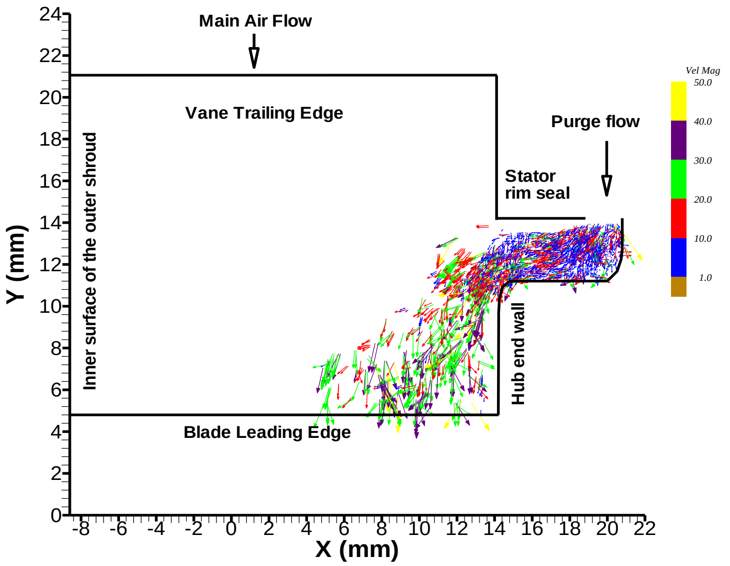

Fig 3.10 Ensemble-averaged egress gas velocity vector map for $Re_{vax} = 9.32\times10^4$, $Re_\Phi = 4.63\times10^5$, $c_w = 8735$, for Configuration – I rim seal geometry at 1/3rd vane pitch location (dT = 2.0 μs)

The velocity vector maps for Expt Set – II are plotted in Figs (3.11 - 3.14). There are noticeable differences between the egress gas paths in the 1/3rd and 2/3rd vane pitch locations. A possible reason could be that the circumferential velocity (or swirl) imparted to the mainstream gas is higher at the 1/3rd vane pitch location. This higher circumferential velocity causes a stronger radially outward movement of the purge gas.

Comparing Figs (3.8 & 3.11; 3.9 & 3.13) it can be seen that, for higher mainstream gas flow rate, there is a greater radial penetration of the egressing purge gas into the mainstream gas path. The above reason could also be attributed to this. The circumferential velocity (swirl) imparted by the vanes on the mainstream gas will be higher for higher mainstream gas mass flow rate.

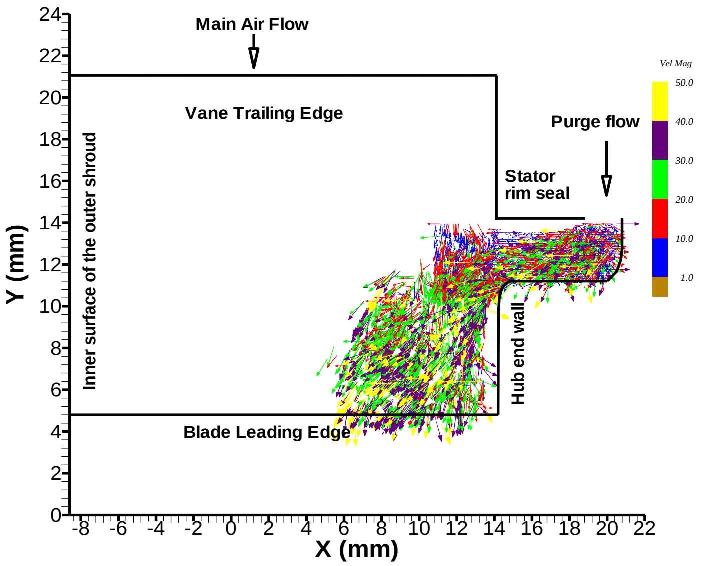

Fig 3.11 Ensemble-averaged egress gas velocity vector map for $Re_{vax} = 1.14\times10^5$, $Re_{\Phi} = 5.86\times10^5$, $c_w = 1653$, for Configuration – I rim seal geometry at 1/3rd vane pitch location (dT = 1.6 μs)

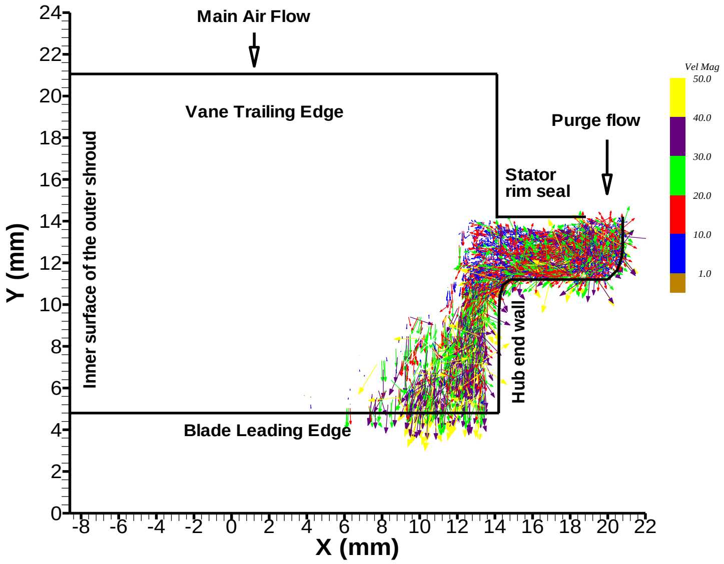

Fig 3.12 Ensemble-averaged egress gas velocity vector map for $Re_{vax} = 1.14\times10^5$, $Re_{\Phi} = 5.86\times10^5$, $c_w = 1653$, for Configuration – I rim seal geometry at **2/3rd** vane pitch location (dT = 1.6 μs)

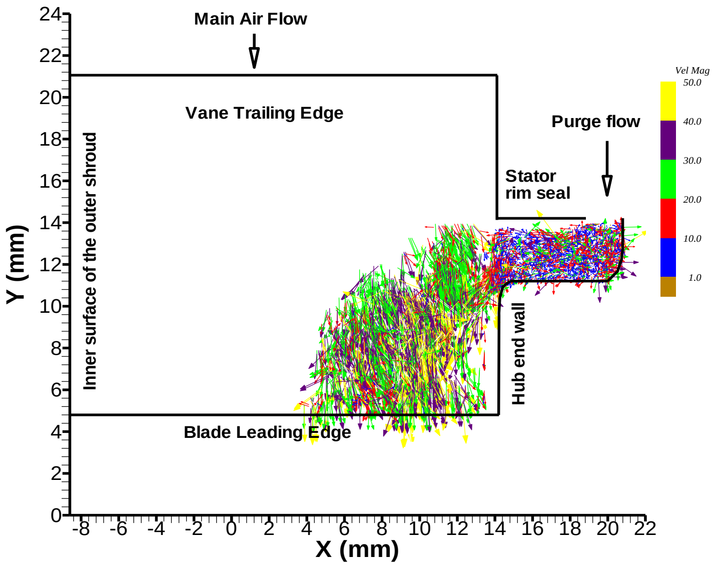

Fig 3.13 Ensemble-averaged egress gas velocity vector map for $Re_{vax} = 1.14 \times 10^5$, $Re_\Phi = 5.86 \times 10^5$, $c_w = 3226$, for Configuration – I rim seal geometry at 1/3rd vane pitch location (dT = 1.6 μs)

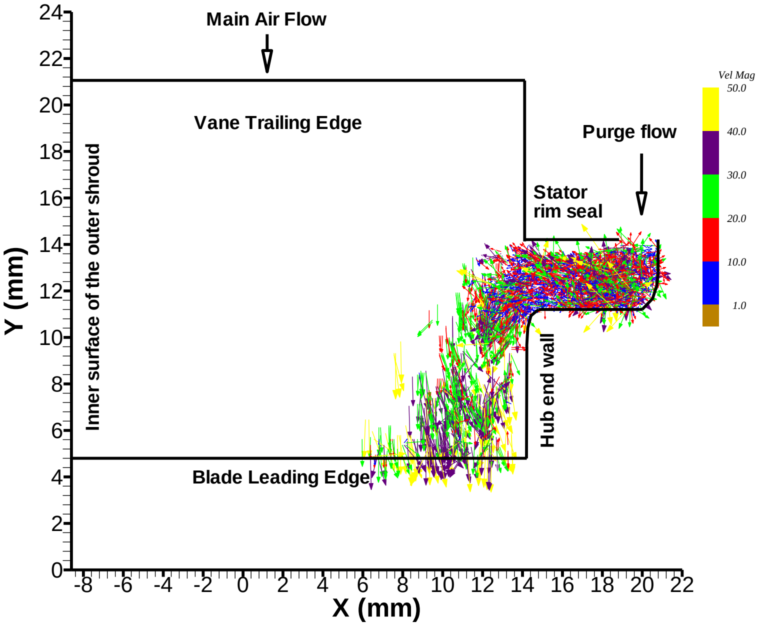

Fig 3.14 Ensemble-averaged egress gas velocity vector map for $Re_{vax} = 1.14 \times 10^5$, $Re_\Phi = 5.86 \times 10^5$, $c_w = 3226$, for Configuration – I rim seal geometry at **2/3rd** vane pitch location (dT = 1.6 μs)

The purge gas egress velocity vector maps were obtained for Configuration – II rim seal geometry as well. The velocity vector map at $1/3^{rd}$ vane pitch location for $Re_{vax} = 1.14\times10^5$, $Re_\varphi = 5.86\times10^5$ and $c_w = 3226$ is shown in Fig (3.15). For this rim seal geometry, the egressing purge gas does not penetrate the main stream gas path as much as Configuration – I, but is directed more towards the lower segments of blade leading edge and intra-blade flow field. This may be an important feature when the near hub-endwall flow field and blade heat transfer are considered.

Apart from this additional feature, all other egress flow characteristics like differences in radial penetration of the purge gas with varying mainstream gas flow rate and purge gas flow rate are similar to the ones that are present in the Configuration – I rim seal geometry.

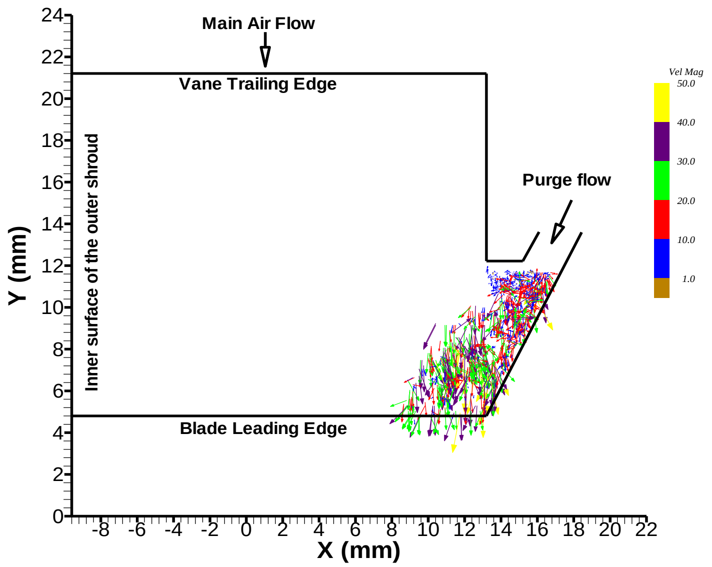

Fig 3.15 Ensemble-averaged egress gas velocity vector map for $Re_{vax} = 1.14\times10^5$, $Re_\Phi = 5.86\times10^5$, $c_w = 3226$, for Configuration – II rim seal geometry at 1/3rd vane pitch location (dT = 1.6 μs)

3.2 1.5-stage Configuration

3.2.1 Experimental Condition

Experiments were carried out for two different rotor speeds and main gas flow rates as shown in Table 3.3. The conditions are specified in terms of non-dimensional parameters: Mainstream gas flow Reynolds number (Re_{vax}), rotor disk rotational speed (Re_{φ}) and non-dimensional mass flow rate of purge gas (c_w). Measurements for main gas ingestion into the aft disk cavity and the purge gas egress flow field (PIV) in the main gas path (in radial-axial plane) at the region between the front blade trailing edge and aft vane leading edge were performed. For the purge gas egress flow field measurements, results are reported only for the conditions that are displayed in **bold** in Table 3.3. The PIV experiments were not performed for the least purge gas flow rate because, at such low flow rate, it was not possible to obtain good seed particle density.

Table 3.3 Experimental Conditions for 1.5-stage turbine configuration

Exp. Set No.	**Mainstream gas Flow rate (Re_{vax})**	**Rotor Speed (Re_{ϕ})**	**β_2 (^{o})**	**Free Disk Pumping Flow rate ($c_{w,fd}$)**	**Purge gas Flow rate (c_w)**		**PIV vane pitch location**	
							$1/3^{rd}$	**Vane leading edge**
III	6.67×10^4	4.93×10^5	35	7844	(a)	822	Not measured	Not measured
					(b)	**1643**	measured	measured
					(c)	2465	measured	measured
					(d)	**3287**	measured	measured
IV	7.12×10^4	5.26×10^5	35	8264	(a)	822	Not measured	Not measured
					(b)	**1643**	measured	measured
					(c)	2465	measured	measured
					(d)	**3287**	measured	measured

3.2.2 Mainstream Gas Ingestion Measurements

Time averaged but spatially resolved main gas ingestion into the aft disk cavity of the 1.5-stage turbine configuration is presented here in terms of sealing effectiveness η (Eq 3.1).

Figures 3.16 and 3.17 respectively show the radial distribution of the sealing effectiveness at the stator surface in the aft disk cavity, for the experiment sets III and IV. Increasing the rotor speed and the main gas flow rate decreases the sealing effectiveness. Also, increasing the purge gas flow rate increases the sealing effectiveness. The distribution of sealing effectiveness within the inner cavity is flat. The sealing effectiveness is much higher in the inner-cavity region than in the rim-cavity region owing to the presence of labyrinth seal. A steep drop in the sealing effectiveness value occurs across the labyrinth seal and significant ingestion into the rim cavity takes place. Such a steep gradient in the η values did not occur for the single-stage turbine configurations. The reason for this is due to the presence of the labyrinth seal. The purge gas exits the labyrinth seal as a jet-like flow which impedes the rim cavity fluid (or ingested mainstream gas) from entering the inner-cavity region. Just as in the case of single-stage turbine configurations, the ingested mainstream gas is mainly confined within the rim-cavity for high purge gas flow rates.

At low purge gas flow rates, there is some ingestion of main air into the inner cavity as well. This is because; the curtain of fluid formed by the jet-like flow of the purge gas is inadequate in sealing the inner cavity at low purge gas flow rate.

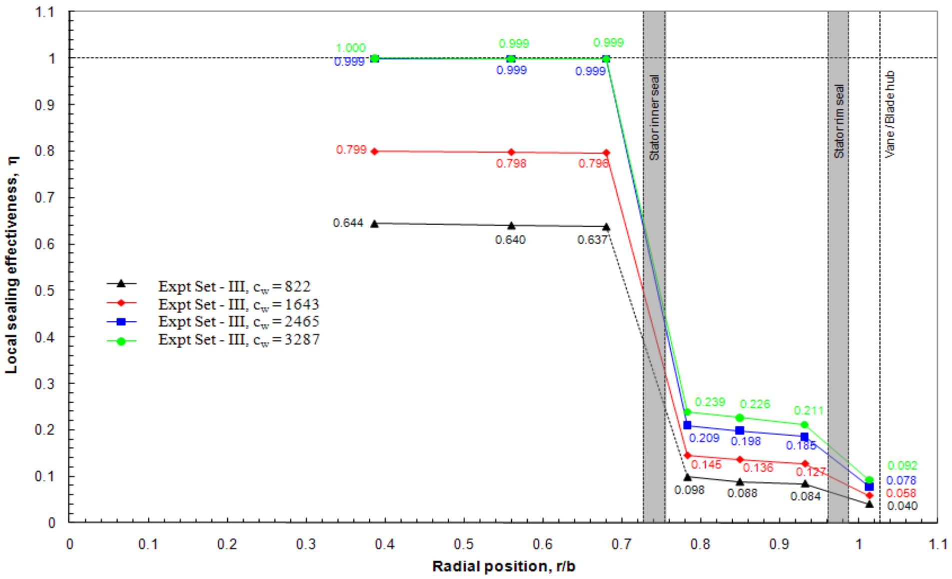

Fig 3.16 Radial distribution of sealing effectiveness within the aft disk cavity, at the stator surface for Expt Set - III

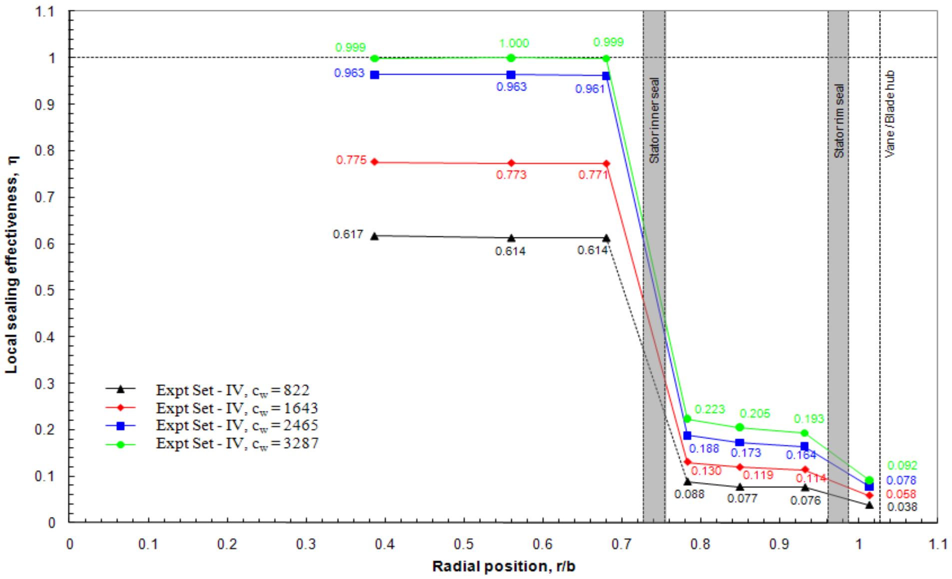

Fig 3.17 Radial distribution of sealing effectiveness within the aft disk cavity, at the stator surface for Expt Set - IV

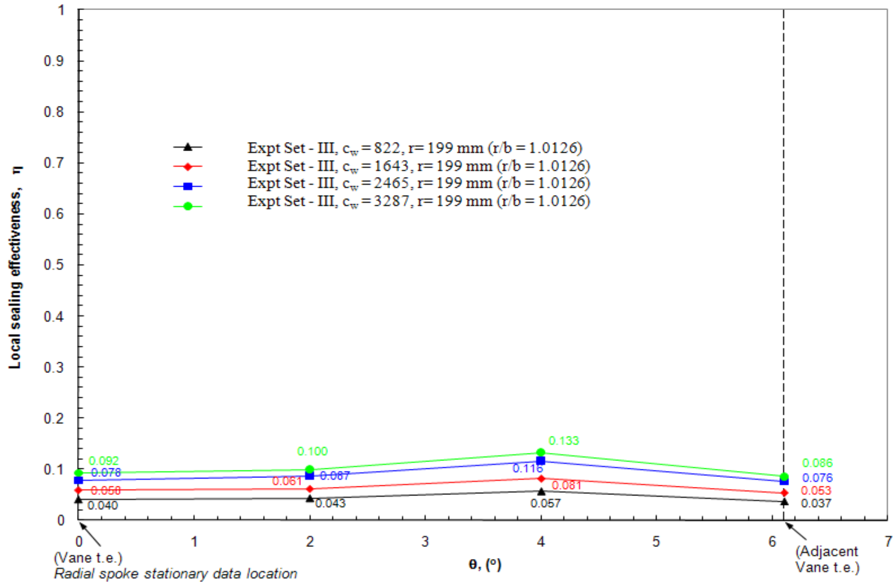

Fig 3.18 Circumferential variation of sealing effectiveness at the stator surface, at r/b = 1.0126 for Expt Set – III

The circumferential variation of the sealing effectiveness (at r = 199 mm, over one vane pitch) on the stator disk surface was measured and is shown in Fig (3.18). No considerable variation could be found circumferentially from the measurements.

3.2.3 Purge Gas Egress-flow field

The egress flow field for the Experimental Set – III, at 1/3rd aft vane pitch location is shown in Figures (3.19 and 3.20). A higher radial penetration of the purge gas into the main gas path is seen for higher purge gas mass flow rate. The velocity of the purge gas in the axial gap between the rim seals is lower compared to the main stream gas path region, where it mixes with the high velocity main stream gas.

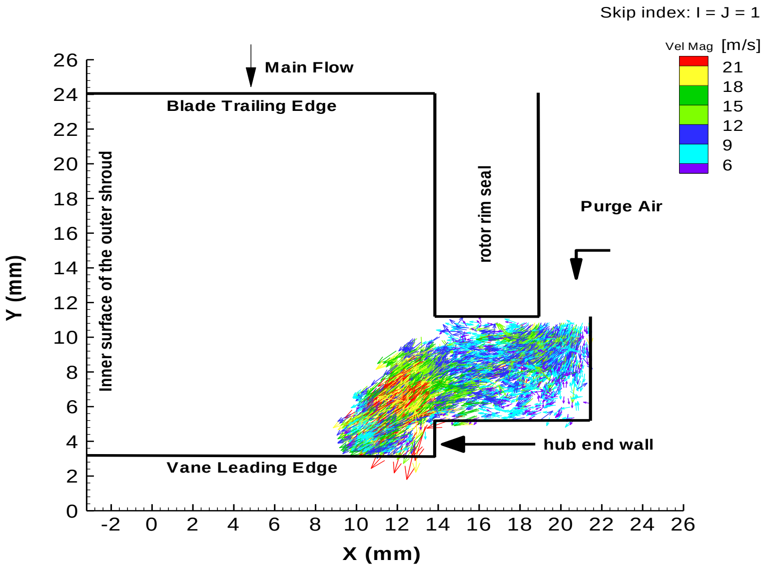

Fig 3.19 Ensemble-averaged egress gas velocity vector map for $Re_{vax} = 6.67\times10^4$, $Re_{\Phi} = 4.93\times10^5$, $c_w = 1643$, at 1/3rd aft vane pitch location (dT = 3.0 μs)

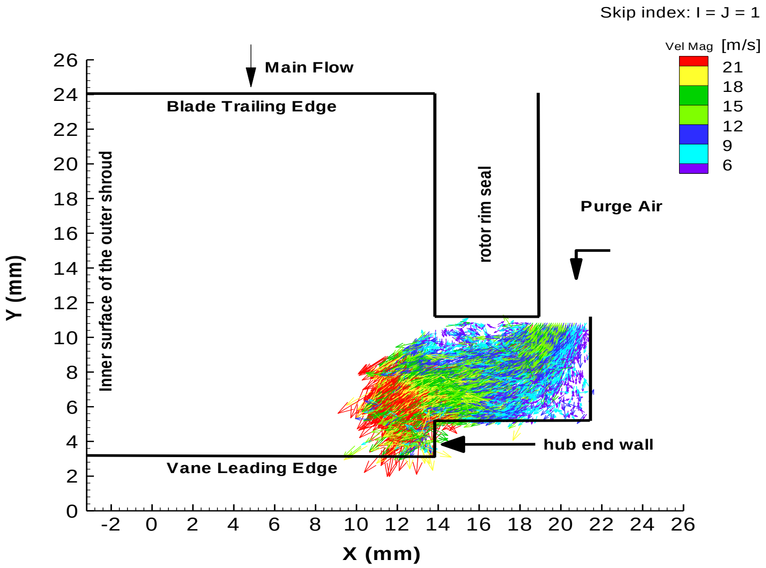

Fig 3.20 Ensemble-averaged egress gas velocity vector map for $Re_{vax} = 6.67\times10^4$, $Re_{\Phi} = 4.93\times10^5$, $c_w = 3287$, 1/3rd aft vane pitch location (dT = 3.0 μs)

Figures (3.21 and 3.22) show the purge gas egress velocity map for Experimental Set IV for the 1/3rd vane pitch location. It is seen that, for the higher mainstream gas mass flow rate, the radial penetration of the purge gas into the mainstream gas path is lower. This is opposite to the trend observed for the single-stage turbine configuration. This is because, in this configuration, the circumferential variation of the swirl imparted by the front vanes are dissipated across the rotor blades and hence in the region between the front rotor and the aft stator, the higher mainstream gas mass flow rate, (higher axial momentum) blocks the purge gas from penetrating into the mainstream gas path.

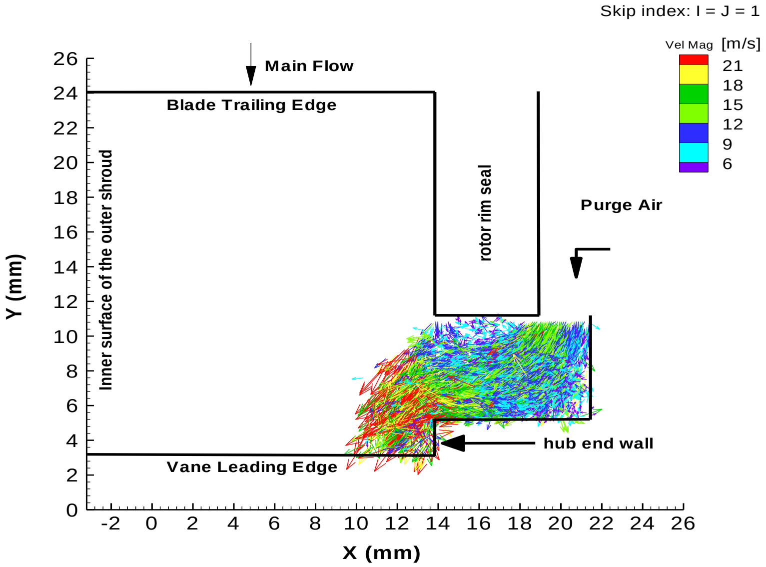

Fig 3.21 Ensemble-averaged egress gas velocity vector map for $Re_{vax} = 7.12\times10^4$, $Re_\Phi = 5.26\times10^5$, $c_w = 1643$, at 1/3rd aft vane pitch location (dT = 3.0 μs)

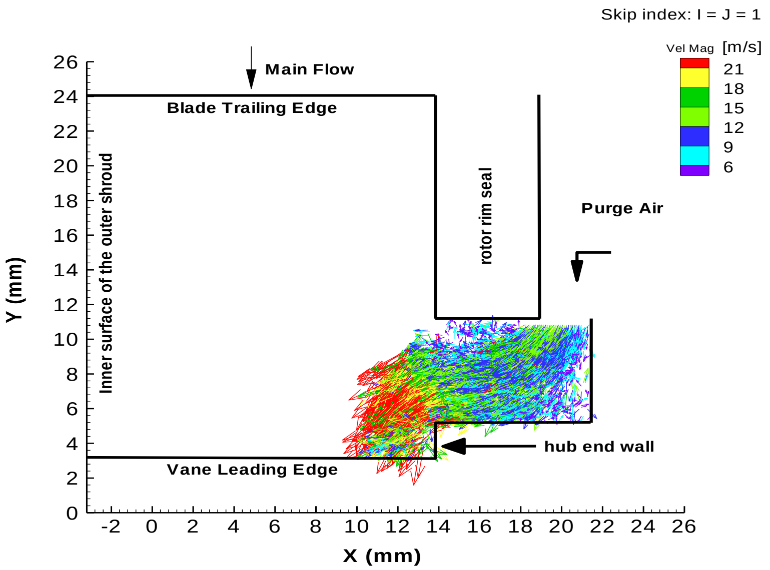

Fig 3.22 Ensemble-averaged egress gas velocity vector map for $Re_{vax} = 7.12\times10^4$, $Re_\Phi = 5.26\times10^5$, $c_w = 3287$, at 1/3rd aft vane pitch location (dT = 3.0 μs)

The Fig (3.23) shows the radial velocity of the purge egress gas (averaged over the radial co-ordinate) within the main stream gas path for the two different main stream gas flow rate. It is seen that, for higher mainstream gas mass flow rate, the radial velocity of the egressing purge gas is lower, which is in direct correlation to the above stated feature.

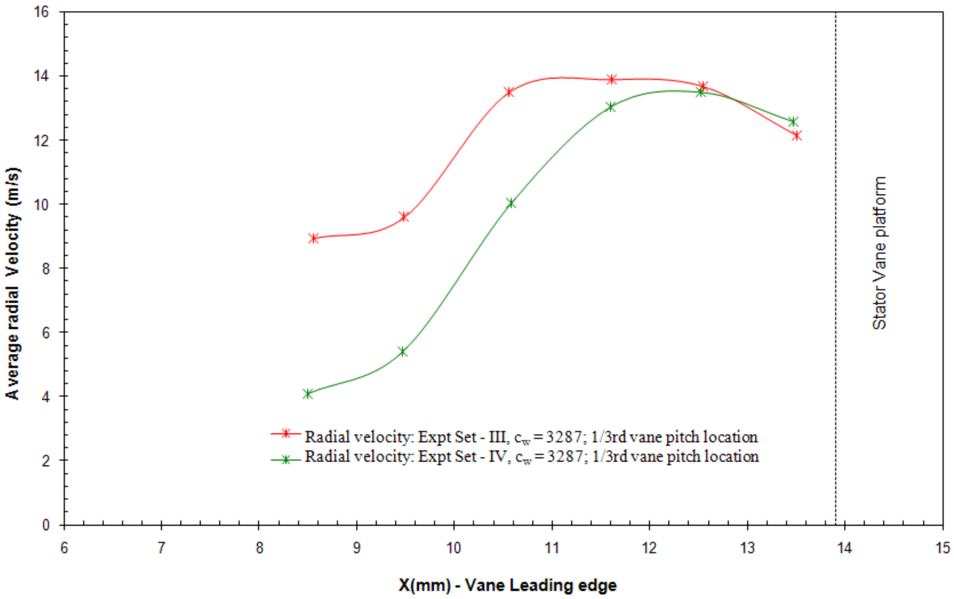

Fig 3.23 Comparison of average radial velocity (from ensemble-averaged plots) at the 1/3rd aft vane pitch location, for different mainstream gas mass flow rate.

The Figs (3.24 and 3.25) show the purge gas egress flow velocity map for the Experimental Set – III at the aft vane leading edge location. There are significant differences between the egress trajectories at the 1/3rd vane pitch and vane leading edge positions. At the 1/3rd vane pitch, the purge gas remains in the PIV measurement plane as it flows into the main gas path whereas at the vane leading edge position, the purge gas moves out of the measurement plane once it enters the main gas path. A possible reason is that at the latter position the main gas has to flow around the vane leading edge because of the higher pressure that develops upstream of the leading edge, this giving rise to an additional tangential movement of the air. The purge air follows suit, flowing around the vane leading edge plane and hence out of the PIV measurement plane.

The flow field within the axial gap between the rim seals is also different. Unlike the 1/3rd vane pitch location, where a purge gas egressing flow is seen, at the vane leading edge location, a re-circulation region is seen. This shows how the purge egress flow field varies based on the circumferential locations of vanes and blades.

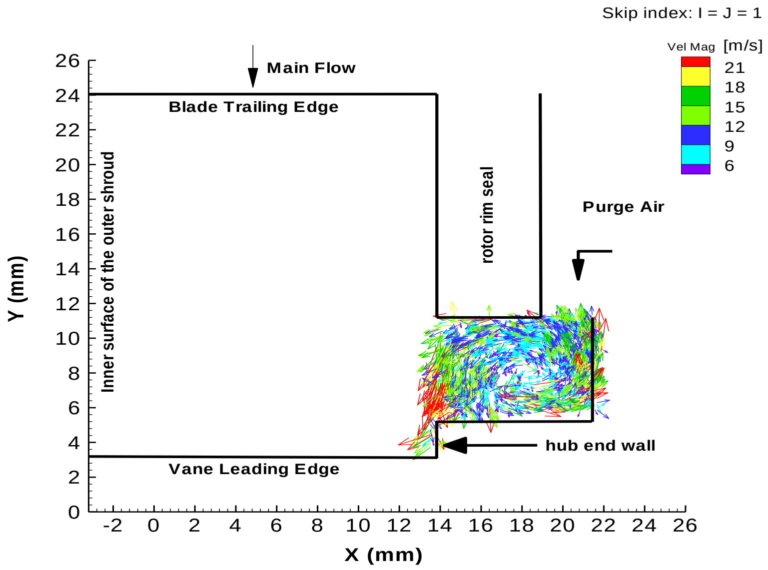

Fig 3.24 Ensemble-averaged egress gas velocity vector map for $Re_{vax} = 6.67\times10^4$, $Re_\Phi = 4.93\times10^5$, $c_w = 1643$, at the aft vane leading edge location (dT = 3.0 µs)

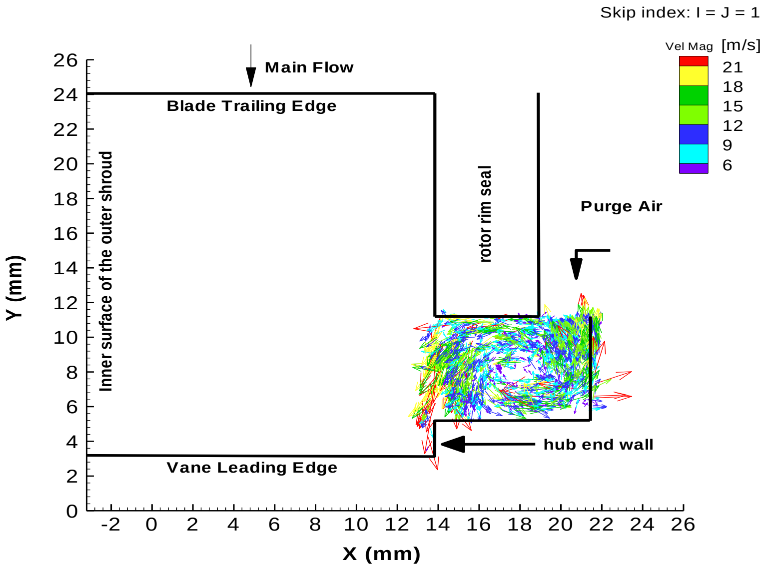

Fig 3.25 Ensemble-averaged egress gas velocity vector map for $Re_{vax} = 6.67\times10^4$, $Re_\Phi = 4.93\times10^5$, $c_w = 3287$, at the aft vane leading edge location (dT = 3.0 μs)

Chapter 4

CONCLUDING REMARKS

Experimental procedures and measurement results of time-average main gas ingestion into the cavities using the tracer gas (CO_2) technique, and ensemble-averaged trajectories of the purge gas flowing out through the rim seal gap into the main gas path using particle image velocimetry were presented. The experiments were performed on model single-stage and 1.5-stage axial-flow air turbines. Three different rim seal configurations, viz., axially overlapping radial clearance rim seals for the single-stage turbine rotor-stator cavity and 1.5-stage turbine aft-cavity, and a rim seal with angular clearance for the single-stage turbine cavity were studied. All the cavities were provided with an inner seal (labyrinth seal for 1.5-stage aft-cavity) radially inboard in the cavity which essentially divided each cavity into an inner cavity and a rim cavity.

The experiments were carried out for several main gas and purge gas flow rates as well as rotor speeds. For each experiment, initially, the time-average static pressure distributions in the main gas path and within the rotor-stator cavity were obtained to ensure that nominally steady flow had been achieved. The static pressure distribution in the main gas path varied circumferentially in a periodic fashion with the period equaling the vane pitch.

Single-stage turbine rim seal configurations

The sealing effectiveness of the rim seals was determined from main gas ingestion measurements. Decreasing the main gas flow rate and rotor speed, and increasing the purge gas flow rate resulted in an increase in the sealing effectiveness, i.e., a decrease in the amount of main gas ingested into the cavity. Significant ingestion of the main gas into the rim cavity occurred only at the lower purge gas flow rates. The inner cavity was almost completely sealed by the inner seal for all purge gas flows. The sealing effectiveness values (both within the rim cavity and the inner cavity) did not vary much for the two rim seal configurations; i.e., both the rim seals performed equally well. Axially, within the rim cavity, sealing effectiveness value was highest at the rotor disk surface and the least at the stator disk.

The purge gas flow egressing through the rim seal gap into the main gas stream, in the region between vane row and the blade row, was imaged using PIV. The time-resolved and ensemble-averaged velocity vector maps were obtained at two vane-pitch locations. The egress flow trajectory was found to be dependent on the configuration of the rim seal, the purge air and main air flow rates, and the azimuthal position within a vane pitch.

1.5-stage turbine configurations

Main gas ingestion into the aft-disk cavity was measured. The measurements showed a steep decrease in the sealing effectiveness value across the labyrinth seal situated between the inner cavity and the rim cavity. This could be attributed to a radial jet-like flow of the purge gas formed by the labyrinth seal that effectively sealed the inner cavity. The jet-like flow impeded the ingested main gas from travelling into the inner cavity at high purge air flows; the ingested main gas was confined within the rim-cavity. At low purge gas flows, significant ingestion occurred in the inner cavity as well.

For the 1.5-stage turbine, the purge gas egressing from the aft-disk cavity was imaged in the region between vane and blade rows using PIV. The images were obtained at two different vane pitch locations. Similar to the single-stage turbine, the purge gas egress trajectory and velocity field were found to depend on the many factors mentioned earlier.

Using the PIV technique, it should be possible to tailor the rim seal configuration to the desired fluid-mechanical and heat transfer effects of the purge air on the downstream vanes and hub endwall.

REFERENCES

Adrian, R.J., 1991, “Particle-Imaging Techniques for Experimental Fluid Mechanics”, Annual Review of Fluid Mechanics, Vol.23, pp.261-304

Cao, C., Chew, J.W., Millington, P.R., and Hogg, S.I., 2003, “Interaction of Rim Seal and Annulus Flows in an Axial Flow Turbine”, ASME Paper no., GT-2003-38368.

Gallier, K.D., Lawless, P.B., and Fleeter, S., 2000, “Investigation of Seal Purge Flow Effects on the Hub Flow Field in a Turbine Stage Using Particle Image Velocimetry,”AIAA Paper 2000-3370.

Ganesan, S., 2007, “Flow Field in a Rotor-Stator Disk Cavity with and Without Pre-swirled Secondary Air”, M.S., Thesis, Arizona State University.

Gentilhomme, O., Hills, N.J., Chew, J.W., and Turner, A.B., 2002, “Measurement and Analysis of Ingestion through a Turbine Rim Seal,” ASME Paper GT-2002-30481.

Green, T. and Turner, A. B., 1994, “Ingestion into the Upstream Wheelspace of an Axial Turbine Stage,” ASME Journal of Turbomachinery, Vol. 116, pp. 327-332.

Jakoby, R., Zierer, T., Lindblad, K., Larsson, J., deVito, L.,Bohn, D. E., Funcke, J., and Decker, A., 2004, "Numerical Simulation of the Unsteady Flow Field in an Axial Gas Turbine Rim Seal Configuration," ASME Paper GT2004-53829.

Johnson, B.V., Mack, G.J., Paolillo, R.E., and Daniels, W.A., 1994, "Turbine Rim Seal Gas Path Flow Ingestion Mechanisms," AIAA Paper 94-2703.

McLean, C., Camci, G., and Glezer, B., 2001, “Mainstream Aerodynamic Effects Due to Wheelspace Coolant Injection in a High-Pressure Turbine Stage: Part 1: Aerodynamic Measurements in the Stationary Frame”, ASME J. Turbomach., 123(4), pp. 687-696.

Mei, R., 1996, “Velocity Fidelity of Flow Tracer Particles”, Experiments in Fluids, 22, pp. 1-13.

Murphy, M.J., 2009, “Development of an Ultra-High Speed Dynamic Witness-Plate Particle Image Velocimetry for Micro Detonator Study”, Ph.D. Thesis, Arizona State University.

Narzary, D., 2005, “Experimental Study of Flow Field in a Model Rotor-Stator Disk Cavity”, M.S., Thesis, Arizona State University.

Owen, J.M. and Rogers, R.H., 1989, Flow and Heat Transfer in Rotating-Disc Systems. Vol. I: Rotor-Stator Systems, Research Studies Press, Taunton, United Kingdom.,

Paniagua G., Denos R. and Almeida S., 2004, “Effect of the Hub Endwall Cavity Flow on the Flow-Field of a Transonic High-Pressure Turbine”, ASME Turbo expo [2004], GT2004-53458.

Phadke, U. P. and Owen, J. M., 1988, “Aerodynamic Aspects of the Sealing of Gas-Turbine Rotor-Stator Systems, Parts 1,2 & 3”, International Journal of Heat and Fluid Flow, Vol. 9(2), pp. 98-117.

Raffel, M., Willert, C., and Kompenhas, J., 1998, Particle Image Velocimetry: A Practical Guide, Springer, Berlin, Germany.

Rolls-Royce, 1986, The Jet Engine, Key Publishing Limited, Stamford, United Kingdom

Roy, R.P., Devasenathipathy, S., Xu, G., and Zhao, Y., 1999, “A Study of the Flow Field in a Model Rotor-Stator Disk Cavity”, ASME Paper 99-GT-246

Roy, R.P., Xu, G., and Feng, J., 2000, “Study of Main-Stream Gas Ingestion in a Rotor-Stator Disk Cavity”, AIAA Paper 2000-3372

Roy, R.P., Xu, G., Feng, J., and Kang, S., 2001, “Pressure Field and Main Stream Gas Ingestion in Rotor Stator Disk Cavity”,ASME Paper 2001-GT-564

Roy, R.P., Feng, J., Narzary, D., and Paolollo, R.E., 2005, “Experiment on Gas Ingestion Through Axial-Flow Turbine Rim Seals”, ASME *Journal of Engineering for Gas Turbines and Power,* Vol. 127. 127, pp.573-582.

Roy, R.P., Zhou, D.W., Ganesan, S., Wang, C-Z., Paolollo, R.E., and Johnson, B.V., 2007, “The Flow Field and Main Gas Ingestion in a Rotor-Stator Cavity”, ASME Paper GT2007-27671

Zhou, D.W., Roy, R.P., Wang, C.Z., and Glahn, G.A., 2009, “Main gas Ingestion in a Turbine Stage for Three rim Cavity Configurations”, ASME Turbo Expo 2009, GT2009-59851.

APPENDIX A

IMAGE CORRECTION PROCEDURE

Image Correction Procedure

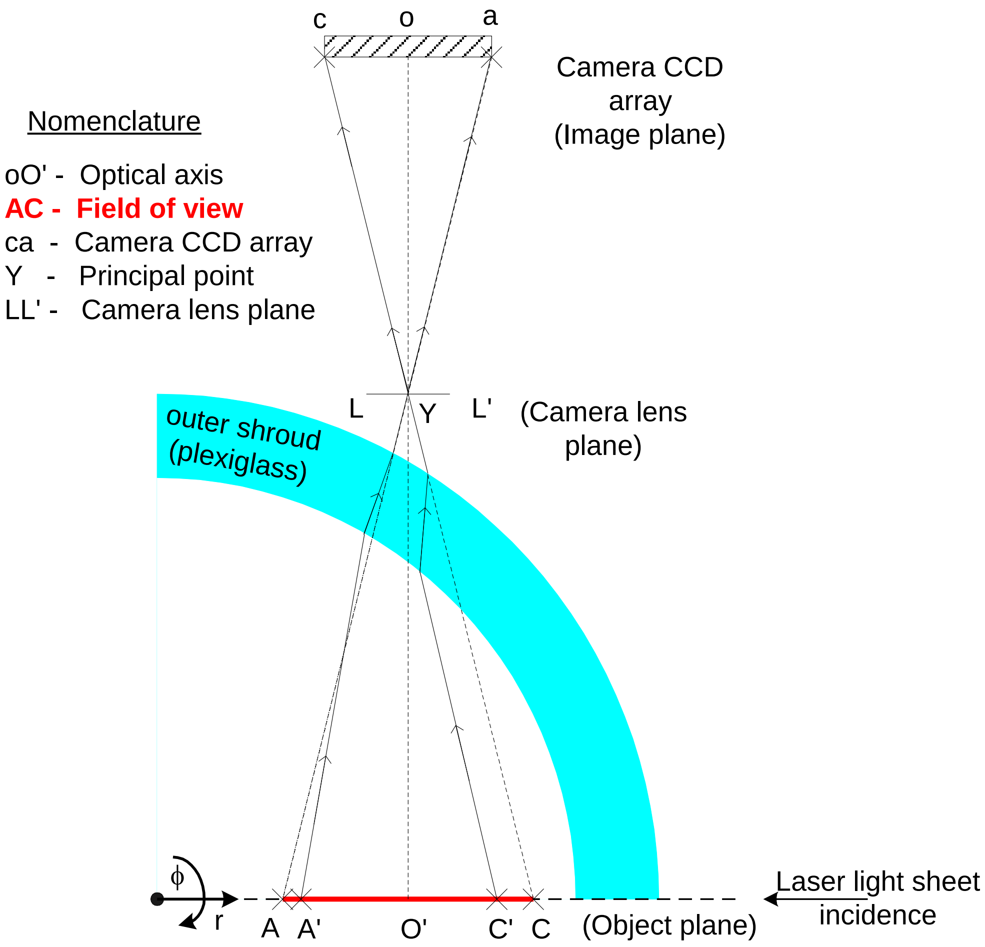

Fig A.1 Light ray refraction through the outer shroud Plexiglass

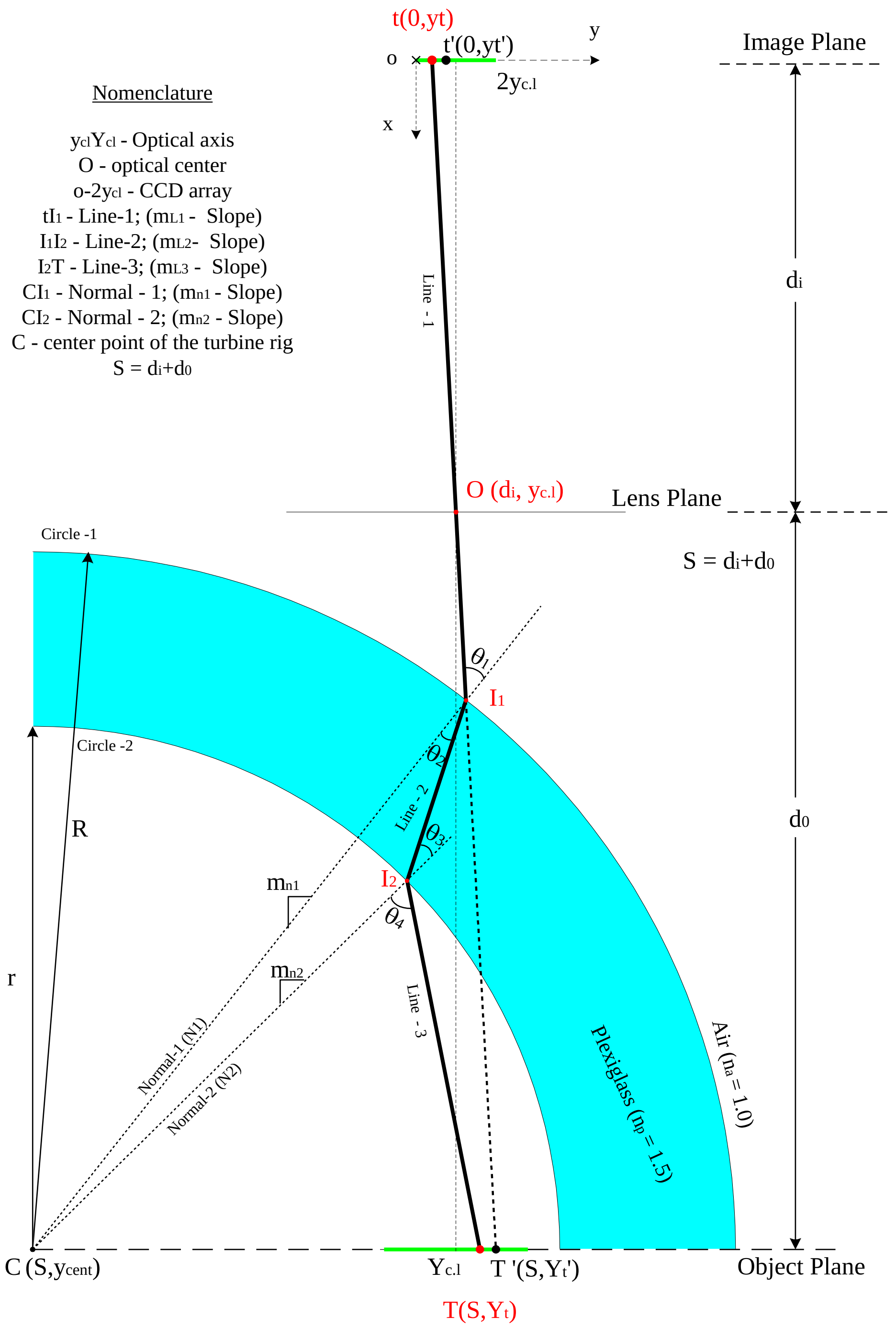

Fig A.2 Co-ordinate system for image correction.

From Fig A.1, AC is the Field of view (FOV). Since the camera images the field of view through the curved plexiglass outer-shroud, the image, as seen by the camera contains distortion due to refraction of light as it passes through media of differing refractive indices. This distortion is one-dimensional and is along the radial co-ordinate only. When the camera views through the outer shroud the actual FOV - AC becomes A'C' (i.e the point A seems to be present at A' and C at C'). This distortion is non-uniform along the radial direction because of the varying shroud thickness that rays from different points along AC passes through.

This distortion can be corrected mathematically similar to the procedure developed by (Murphy 2009). In this section, the mathematical correction procedure pertaining to this PIV system used in this work is explained.

Ray tracing technique along with simple co-ordinate geometry is employed to find the 1-D mapping function to correct for the distortion. From (Murphy 2009), the compound camera lens (Nikon Nikkor 105 mm) of the imaging system can be considered to be a thin lens (since it can be assumed that the camera compound lens is made of many thin lenses) and thus make use of the Gaussian Lens equation

$$\frac{1}{f}=\frac{1}{d_0}+\frac{1}{d_i} \tag{A.1}$$

Where d_0 and d_i are the respective object and image distances measured from the lens-plane (effective lens plane in case of the compound lens) to the object and image planes. Considering the compound lens as a thin lens helps in simplifying the derivation of the 1-D refraction mapping function.

It must be understood that, light rays from all the different points along the object plane that gets focused onto the image plane (CCD array of the camera) pass through the optical center – O (Fig 2). This information helps in tracing a ray from a point on the image plane to find out its corresponding object plane point (both with and without refraction by outer-shroud).

Let us consider a general pixel point $t(0,y_t)$ on the CCD array at which an image gets formed in the absence of the outer shroud. Our aim is to find the pixel point $t'(0,y_t')$ at which the aforementioned image gets formed with the outer shroud in place. If this is achieved, then for each pixel (t') of the distorted image, one would be able to find the pixel point (t) at which that image would be formed without the outer-shroud i.e, this would help in correcting the distorted image.

Let us consider a general pixel point $t(0,y_t)$ as shown in Fig A.2. Tracing a ray from it through the optical center leads to $T'(S,Y_t')$ in the object plane i.e, in the absence of outer-shroud, the point $T'(S,Y_t')$ gets imaged at pixel point t on the image plane. When the outer shroud refractions are taken into consideration, the ray from pixel point t leads to point $T(S,Y_t)$ which is the perceived location of $T'(S,Y_t')$ as seen from the image plane. This shift $(Y_t' - Y_t)$ is called the object plane shift and this value is subsequently used to find the pixel point $t'(0,y_t')$ at which the image (formed at point t in the absence of outer shroud) gets formed in the presence of outer shroud. The equations that follow are used to find the object plane points T and T' for a general point t in the image plane which finally leads to t'.

All the equations are constructed with reference to Fig 2. Here the point 'o' in the image plane (LHS end of the camera CCD array) is selected as the origin. The slope of line-1(m_{L1}) from the point t to the optical center O and its equation are as given below.

$$m_{L1} = \frac{y_{CL}-y_t}{d_i} \quad \text{(A.2a)}$$

$$\alpha_{L1} = \tan^{-1}(m_{L1}) = \tan^{-1}(\frac{y_{CL}-y_t}{d_i}) \quad \text{(A.2b)}$$

$$y = y_t + (\frac{y_{CL}-y_t}{d_i})x \quad \text{(A.2c)}$$

Since the outer surface of the plexiglass outer shroud is circular (Radius – R), the equation of it is as below. The intersection point (I_1) of Line-1 with the outer surface of the plexiglass is found by solving equations (A.2c) and (A.3a).

$$(x-S)^2 + (y-y_{cent})^2 = R^2 \quad \text{(A.3a)}$$

$$(1+m_{L1}^2)x^2 + (2y_t m_{L1} - 2y_{cent}\, m_{L1} - 2S)x + (S^2 + y_t^2 + y_{cent}^2 - 2y_t y_{cent} - R2=0 \quad \text{(A.3b)}$$

$$a_{11} = (1+m_{L1}^2) \quad \text{(A.3c)}$$

$$b_{11} = (2y_t m_{L1} - 2y_{cent}\, m_{L1} - 2S) \quad \text{(A.3d)}$$

$$c_{11} = (S^2 + y_t^2 + y_{cent}^2 - 2y_t y_{cent} - R^2) \quad \text{(A.3e)}$$

Solving the above quadratic for the intersection points provides the co-ordinates

of I_1:

$$x_{I1} = \frac{-b_{11} - \sqrt{b_{11}^2 - 4a_{11}c_{11}}}{2a_{11}} \tag{A.3f}$$

$$y_{I1} = \left(\sqrt{R^2 - (x_{I1} - S)^2}\right) + y_{cent} \tag{A.3g}$$

Refraction occurs at the intersection point I_1. To find the angle of incidence (θ_1) the surface normal to Circle-1 at the intersection point is found out. Then, the slope of the surface normal (m_{n1}) and the incidence angle (θ_1) are found as below.

$$m_{n1} = \frac{y_{I1} - y_{cent}}{x_{I1} - S} \tag{A.4a}$$

$$\alpha_{N1} = 180 + \tan^{-1}(m_{n1}) \tag{A.4b}$$

$$\theta_1 = 180 - (\alpha_{N1} - \alpha_{L1}) \tag{A.4c}$$

Using the incidence angle, refractive index value for plexiglass ($n_p = 1.5$) and air ($n_a = 1.0$) and using Snell's law (A.5a), the angle of refraction is calculated. This is used to find the slope and the equation for Line-2. (Where α_{L2} is the angle made by Line-2 with the x-axis.)

$$n_a \sin\theta_1 = n_p \sin\theta_2 \tag{A.5a}$$

$$\theta_2 = \sin^{-1}\left(\frac{n_a \sin\theta_1}{n_p}\right) \tag{A.5b}$$

$$\alpha_{L2} = \theta_2 + \alpha_{L1} - \theta_1 \tag{A.5c}$$

$$m_{L2} = \tan(\alpha_{L2}) \tag{A.5d}$$

$$y = m_{L2} + (y_{I1} - m_{L2}x_{I1}) \tag{A.5e}$$

The equation of Line-2 is used to find the intersection point I_2 by solving equation (A.5e) and the equation for the inner surface of outer shroud (A.6a). Steps similar to the ones carried out for I_1 and Circle-1 are done for I_2 and Circle-2 to obtain the angle of incidence (θ_3) and angle of refraction (θ_4).

$$(x - S)^2 + (y - y_{cent})^2 = r^2 \tag{A.6a}$$

$$(1 + m_{L2}^2)x^2 + (2y_{I1}m_{L2} - 2y_{cent}\, m_{L2} - 2S - 2m_{L2}^2 x_{I1})x + (S^2 - r^2 + (y_{I1} - x_{I1}m_{L2} - y_{cent})^2) \tag{A.6b}$$

$$a_{22} = (1 + m_{L2}^2) \tag{A.6c}$$

$$b_{22} = (2y_{I1}m_{L2} - 2y_{cent}\, m_{L2} - 2S - 2m_{L2}^2 x_{I1}) \tag{A.6d}$$

$$c_{22} = (S^2 - r^2 + (y_{I1} - x_{I1}m_{L2} - y_{cent})^2) \tag{A.6e}$$

$$x_{I2} = \frac{-b_{22} - \sqrt{b_{22}^2 - 4a_{22}c_{22}}}{2a_{22}} \tag{A.6f}$$

$$y_{I2} = \left(\sqrt{r^2 - (x_{I2} - S)^2}\right) + y_{cent} \tag{A.6g}$$

$$m_{n2} = \frac{y_{I2} - y_{cent}}{x_{I2} - S} \tag{A.7a}$$

$$\alpha_{N2} = 180 + \tan^{-1}(m_{n2}) \tag{A.7b}$$

$$\theta_3 = 180 - (\alpha_{N2} - \alpha_{L2}) \tag{A.7c}$$

$$n_p \sin\theta_3 = n_a \sin\theta_4 \tag{A.8a}$$

$$\theta_4 = \sin^{-1}\left(\frac{n_p \sin\theta_3}{n_a}\right) \tag{A.8b}$$

The slope and equation for Line-3 are obtained and this equation is used to obtain point T(S,Y$_t$) from equation (A.9). And point T'(S,Y$_t$') which is the actual location in the absence of outer shroud is obtained from equation(A.10).

$$\alpha_{L3} = \theta_4 + \alpha_{L2} - \theta_3 \tag{A.8c}$$

$$m_{L3} = \tan(\alpha_{L3}) \tag{A.8d}$$

$$y = y_{I2} + m_{L3}(S - x_{I2}) \tag{A.8e}$$

$$Y_t = y_{I2} + m_{L3}(S - x_{I2}) \tag{A.9}$$

$$Y_t' = y_t + m_{L1}S \tag{A.10}$$

Having found the co-ordinates of points T and T' which are the perceived and actual locations on the object plane corresponding to the image plane point t; we find the object plane shift as below. This object plane shift is converted to image plane shift using the Magnification and into pixel length scales by making use of the physical dimension of a pixel for the camera used. (1 pix = 7.4μm = d_p).

$$Object\ Plane\ Shift = Y_t' - Y_t \tag{A.11}$$

$$Image\ Plane\ Shift = M(Y_t' - Y_t) \tag{A.12}$$

$$Image\ Plane\ Shift\ (in\ pixels) = \frac{M(Y_t' - Y_t)}{d_p} \tag{A.13}$$

As explained earlier, let us consider that in the absence of the Plexiglass outer shroud, an image forms at the pixel point t. Then the pixel point t' where that image would be formed in the presence of the Plexiglass outer shroud (because of refraction effects; 1-D alone, such that t' and t lie in the same row of the camera CCD array) is found out using the Image Plane Shift obtained above.

$$y_t - y_t' = \frac{M(Y_t' - Y_t)}{d_p}\left(= location\ {}^{w}/_{0}\ shroud - location\ with\ shroud\right) \tag{A.14}$$

$$y_t' = y_t - \frac{M(Y_t' - Y_t)}{d_p} \tag{A.15}$$

Each digital image is an array of intensity values (each pixel stores a particular intensity value). Thus in this case, to correct an image, instead of modifying the existing distorted image, we generate a new image devoid of any distortion from the intensity values of the distorted image. Thus for any general pixel point t of a new blank image, using the above algorithm we find the image plane shift. This information is subsequently used to find out the corresponding pixel point in the distorted image - t’ at which the image gets formed (which in the absence of the outer shroud would have been formed at t).

Thus a table of y_t’ and y_t (for each pixel point in t) is formed and this is used to generate the corrected image from the distorted image. The figure displayed (Fig A.3) below gives a pictorial representation of the generation of a corrected image from the distorted image.

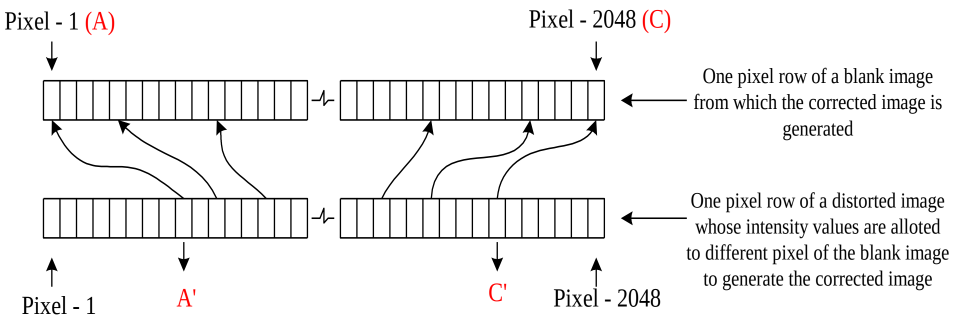

Fig A.3 A pictorial representation of generation of corrected image. The red labels (A&C) are corresponding to the labeling followed in Fig A.1

In order to validate this procedure, a target image (Edmund Optics – NT38-710) was imaged both with and without the outer shroud, at the same magnification that was used for the experiments. The resulting images are displayed below.

(a) without outer shroud

(b) with outer shroud

Fig A. 4 Image of a Target

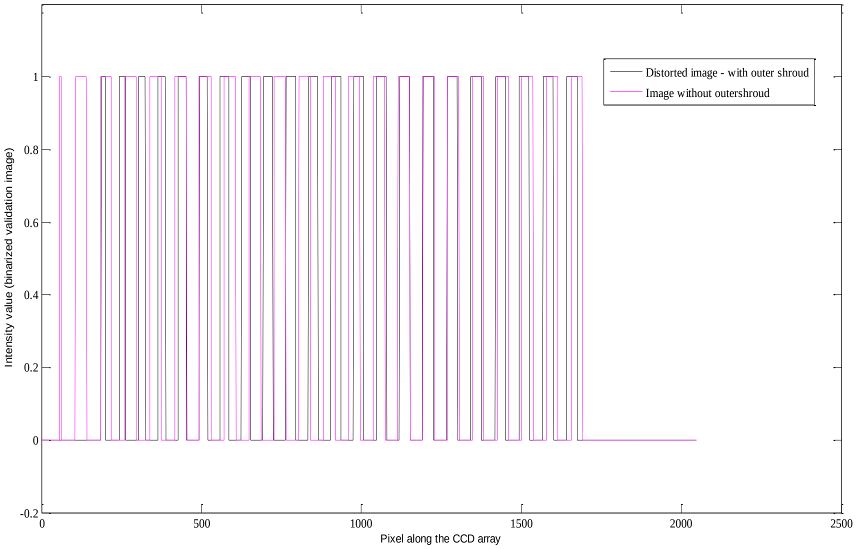

(a) For the complete row

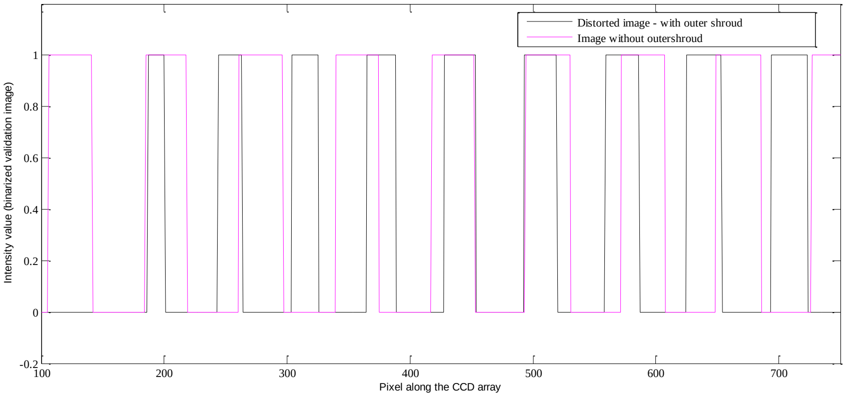

(b) Zoomed in view of (a)

Fig A. 5 Intensity histogram for one pixel row for Fig A.4

Intensity histograms for one pixel row of the validation images (Figs A.4) were plotted (Fig A.5). These histograms were then used to measure the image plane shift for the validation images. Subsequently, these measured values of image plane shift are plotted against the pixels across the image plane and are compared to those obtained from the 1D mapping procedure (Fig A.6) and is found to compare very well. This proves the applicability of the procedure developed above to correct the PIV raw images.

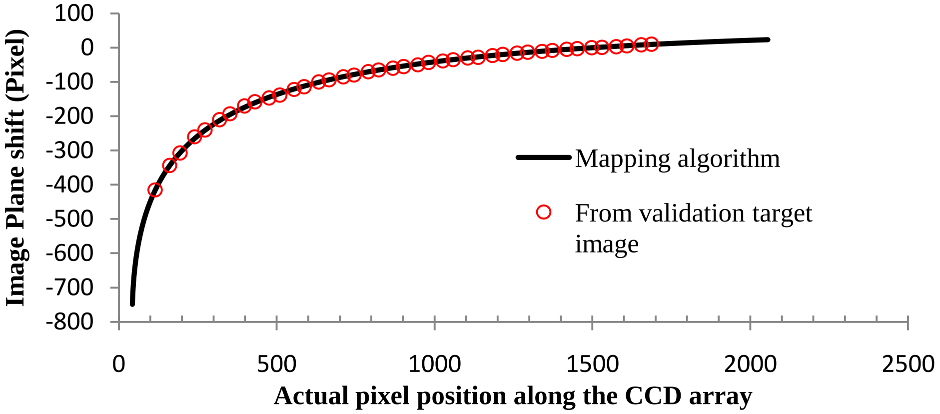

Fig A.6 Image plane shift calculated from the refraction mapping procedure and measured from the validation image.

APPENDIX B

SEED PARTICLE DYNAMICS

Seed particle dynamics

The accuracy of PIV measurements depends on the ability of the seed particles to follow the fluid flow. The seed particle's flow in a particular fluid is described by the dimensionless Stokes (Sk) number. Generally, if the Stokes number is lesser than unity, then the particle will faithfully follow the fluid flow. The Stokes number is defined below in Equation B.1

$$Sk = \frac{\tau_p * V_f}{d_c} \tag{B.1}$$

where V_f is the fluid velocity, d_c is the fluid flow characteristic length and τ_p is the particle time constant, which is the time required for the particle to respond to the changes in fluid velocity. The particle time constant is calculated from the expression shown in Equation B.2

$$\tau_p = \frac{(\rho_p - \rho_f)d_p^2}{18\rho_f \nu_f} \tag{B.2}$$

where ρ_p , d_p are the particle density and diameter respectively and ρ_f , ν_f are the fluid density and kinematic viscosity.

Additionally, to follow the fluid acceleration, the seed particles must slip with respect to the fluid in order to generate the required drag force. This slip velocity (of particle with respect to fluid) leads to errors in the PIV measurements as the seed particles tend to lag the fluid velocity and one tries to minimize this slip velocity (with proper seeding) to improve the measurement accuracy.

In the present work, the purge gas was seeded with the olive oil droplets (seed particles) before its entry into the disk cavity. In this section, the ability of the seed particles to follow the fluid flow is determined by evaluating the Stokes number, and the particle slip velocity, under the effect of cavity-fluid centrifugal acceleration (imparted by the rotation of rotor disk) is also evaluated. This slip velocity (due to centrifugal acceleration) causes the seed particle to move out radially.

The particle slip velocity (v_p – u) due to the cavity-fluid centrifugal acceleration (V^2/r) is given in equation B.3

$$v_p - u = \tau_p * \frac{V^2}{r} \qquad (B.3)$$

The above equations (B.1 to B.3) were obtained from Raffel (1998) and Mei (1996).

A Stokes number << 1, a low particle slip velocity and a low particle time constant ensures that the errors (due to particle slip velocity) in PIV measurements are low. The table (B.1) lists the different parameters of the fluid and seed particles along with the calculated values of particle time constant, Stokes number and particle slip velocity.

The tangential and radial velocities of the cavity-fluid (Purge gas) within the disk cavity, listed in Table B.1 are obtained from Zhou (2009, who used similar turbine stages). The cavity-fluid radial velocity is used in calculating the Stokes number. The rotor-stator gap of 16.5 mm is taken as the cavity flow characteristic length as the purge gas flows out radially through this gap. The purge gas tangential velocity within the disk cavity is used for calculating the particle slip velocity due to cavity-fluid centrifugal acceleration.

Table B.1 Seed particle slip-velocity

Parameter	**Value**	**Unit**
Particle diameter (d_p) (from Diganta 2005)	1.54E-06	m
Particle density (Olive oil at room temperature)	9.15E+02	Kg/m^3
Fluid density (air @ 23°C)	1.19E+00	Kg/m^3
Fluid Kinematic viscosity (air @ 23°C)	1.54E-05	m^2/s
Maximum Purge gas tangential velocity in disk cavity	3.50E+01	m/s
Maximum Purge gas radial velocity in disk cavity	1.50E+01	m/s
Characteristic length scale - cavity fluid flow (rotor-stator gap)	1.65E-02	m
Particle time constant - τ_p	**6.55E-06**	**s**
Stokes Number (Sk)	**5.96E-03**	**no unit**
Particle slip velocity (v_p-u)	**0.0436**	**m/s**

The Stokes number is 0.0059 which is lesser than unity. The value of Stokes number, if calculated using the maximum fluid tangential velocity, can increase to 0.01 also. These lower Stokes numbers may indicate that the particle might follow the fluid flow faithfully. Stokes number lower than these cannot be achieved while using olive oil droplets due to the difference in the densities between oil and air, and the droplet size cannot be reduced further considering its effect on light scattering.

Additionally, the maximum particle slip velocity is around 0.043 m/s. This value has to be compared to the local fluid radial velocity. At some locations radially inboard in the rim cavity, the fluid radial velocities are as low as 1 m/s. At these locations the slip velocity might influence the PIV measurement. At other locations, the particle slip velocity is very low compared to the local fluid velocity, which is acceptable.